Flame Surface Density Measurements and Curvature Statistics for Turbulent Premixed Bunsen Flames

Tyler George Capil

Thesis submitted to the faculty of the Virginia Polytechnic Institute and State University
in partial fulfillment of the requirements for the degree of

Master of Science
In
Mechanical Engineering

Lin Ma, Chair
Weiwei Deng
Pablo Tarazaga

February 7, 2017
Blacksburg,VA

Keywords: flame surface density, flame curvature, CH PLIF, HiPilot burner

Flame Surface Density Measurements and Curvature Statistics for Turbulent Premixed Bunsen Flames

Tyler George Capil

ABSTRACT

In this work, turbulent premixed combustion was analyzed through CH (methylidyne) planar laser induced fluorescence (PLIF). Flame topography measurements in terms of flame surface density and curvature were calculated based on the flame front detected by the CH PLIF signal. The goal of this work was to investigate turbulent flames with extremely high turbulence intensity using a recently developed HiPilot burner (a Bunsen-type burner). The studies were first conducted on a series of piloted jet flames to validate the methodology, and then conducted on the highly turbulent flames generated by the HiPilot burner. All flames were controlled by combusting methane and air under a fuel to air equivalence ratio of $\phi = 1.05$, and the Reynolds number varied from 7,385 to 28,360. Flame surface density fields and profiles for the HiPilot burner are presented. These flame surface density measurements showed an overall decrease with height above the burner. In addition, curvature statistics for the HiPilot flames were calculated and probability density functions of the curvature samples were determined. The probability density functions of curvature for the flames showed Gaussian-shaped distributions centered near zero curvature. To conclude, flame topography measurements were verified on jet flames and were demonstrated on the new HiPilot flames.

Flame Surface Density Measurements and Curvature Statistics for Turbulent Premixed Bunsen Flames

Tyler George Capil

GENERAL AUDIENCE ABSTRACT

Optical diagnostics are powerful techniques that enable the study of turbulent flames without physical interruption. The optical diagnostic technique in this thesis implemented planar laser induced fluorescence. In planar laser induced fluorescence, a laser is used to excite a specific molecular species present within a two-dimensional plane in the flame. The excited species releases the extra energy by emission of light which is the signal captured on a camera. One useful purpose of using optical diagnostics, such as planar laser induced fluorescence, is the ability to image the flame structure of turbulent flames. The flame structure is significant for two reasons. First, the flame structure details how the chemistry of the flame interacts with the turbulent flow field. Second, the flame structure is directly related to the burning rate of the reactants. The primary contribution of this thesis investigated the two-dimensional flame structure of a newly designed burner named the HiPilot burner. However, in order to strengthen the fidelity of the methods for determining certain flame structure quantities a precursive analysis on the classical jet flame was completed. The results acquired show structural measurements of the HiPilot flames which contribute to the repository of data for the combustion community.

ACKNOWLEDGEMENTS

I would like to express my gratitude for my committee members Drs. Lin Ma, Weiwei Deng, and Pablo Tarazaga for their participation and support. Moreover, I would like to give special thanks to Dr. Lin Ma, who has given me the opportunity to explore my passions and has guided me throughout my research.

I would like to thank my fellow members in the Laser Diagnostic Lab who have acclimated me in the research environment and have advised me on some tough problems. Special thanks is given to Yihua Ren who has devoted much time in helping me with my research.

I would like to thank my friends who have always had my back. Without their enduring support, I would not have made it this far. My sincerest gratitude goes to Justin Leyeza, Nicole Navasca, and Katrina Navasca for always being there to talk to and for believing in me.

Lastly and most importantly, I would like to thank my family who has supported me immensely. Thanks to my sister, Adrienne Capil, for always being there for me. To my father and mother, George and Rose Capil, who have always encouraged me to dream big. Thank you for giving me the opportunity to pursue my dreams. I would not be where I am today without you all.

TABLE OF CONTENTS

LIST OF FIGURES

Chapter 1 INTRODUCTION

1.1 Background

In modern power and propulsion producing devices, premixed combustion is often the preferred method compared to non-premixed combustion for a variety of considerations [1]. Premixed combustion involves having both fuel and oxidizer to be mixed before the combustion process. In contrast, non-premixed combustion involves separate streams of fuel and oxidizer just before combustion. The former is the preferred method since premixed combustion is known to cause less toxic pollution products. With the increasing need for energy around the world, combustion of fossil fuels still remains one of the dominant sources of energy. Therefore, much effort is given into understanding the fundamentals of combustion in order to develop power and propulsion devices with enhanced fuel efficiency and reduced emissions.

One of the main challenges of studying turbulent premixed combustion involves developing the experimental diagnostics to study the characteristics of combustion flames without intrusively interrupting the flow [2]. Unlike physical probes which interrupt the target flame (and may become damaged in extreme environments), non-intrusive diagnostics have the benefit of interrogating of the flame without physical interruption. More specifically, much attention has been given to studying the structure of turbulent premixed flames through the use of laser diagnostics. The focus of this study centralizes on the structural aspect of flames through the use of a noninvasive laser diagnostics: planar laser induced fluorescence (PLIF) based on methylidyne (CH) radicals. In particular, this study focuses on the flame surface density and curvature statistics for a recently developed Bunsen-type burner, called the HiPilot burner.

The study of flame surface density and curvature statistics are motivated both by their fundamental value to the understanding of turbulent flames, and also by their relationship to the burning rate [3-5]. The burning rate in combustion is one of the key characteristics of interest both for scientific and industrial considerations. An important model that helps to understand the burning rate is the flamelet model [6]. Under the flamelet assumption, the flame front is composed of an ensemble of thin, locally laminar segments. Inside the thin flame front is the reaction layer where combustion occurs. Furthermore, the flamelet assumption considers the flame to move with a laminar burning velocity. The laminar burning velocity does not depend on flow field characteristics. Instead the laminar burning velocity depends on thermal and chemical characteristics. Based on this model, the burning rate ($\dot{\omega}$, defined as the mean rate of conversion of reactants into products per unit volume) can be described by the following equation [7, 8]:

$$\dot{\omega}(x) = \rho_r S_{L0} I_0 \Sigma(x) \tag{1}$$

where ρ_r is the density of the reactants, S_{L0} is the unstretched laminar burning velocity, I_0 is the stretch factor, and $\Sigma(x)$ is the flame surface density along the axial coordinate [7, 8]. The product of the unstretched laminar burning velocity and the stretch factor is the mean laminar burning velocity. The stretch factor is important as it accounts for strain rates and curvatures along the laminar flamelets.

Another important characteristic of combustion is the turbulent burning velocity, or the local consumption speed of the reactants. The local turbulent burning velocity is highly dependent on the structure and geometry of the flame. Flame topography (or structural) properties can include flame surface density, flame brush thickness, curvature, and others [3]. This work reports the experimental measurements of two of these topography properties: the flame surface density and the flame front curvature. As discussed above, these properties are

directly linked to the determination of the burning rate. The turbulent burning velocity does not depend on local turbulence levels. Instead, the turbulent burning velocity is reliant on the complex geometries of the flame. In particular, wrinkling structures in the flame strongly influence the geometry and turbulent burning velocity of flames. It has been said that the wrinkling downstream of the flame has "memory" on the wrinkling that occurs upstream [3]. Therefore, the structural or geometrical quantities on all parts of the flame are necessary to determine local turbulent burning velocity.

The turbulent burning velocity has been defined in several ways, and there are open questions in this area. Driscoll has provided several definitions of the turbulent burning velocity, none of which are deemed superior to the other [3]. Consequently, the definition of turbulent burning velocity is dependent on the objective of the problem. Since this study focuses on the flame surface density, the most relevant definition of turbulent burning velocity is the local consumption speed. Other work in literature has pointed out that the integral of the flame surface density is proportional to the turbulent burning velocity [3, 8]. More precisely, the turbulent burning velocity, S_T, can be expressed in terms of flame structural quantities as

$$S_T = S_{L0} I_0 \int_{-\infty}^{\infty} \Sigma \, d\eta \tag{2}$$

where S_{L0} is the unstretched laminar burning velocity, I_0 is defined as the stretch factor, Σ is the flame surface density, and η is the coordinate perpendicular to the flame brush. The definition of turbulent burning velocity, S_T, in this case is also called the local consumption speed.

The measurements and statistics obtained in this work are also useful for the validation and calibration of computational models such as large eddy simulations (LES) and direct numerical simulations (DNS) [9-11]. Computational models ultimately are needed to gain an understanding of how the flame interacts with the highly turbulent flow field at a fundamental

level and to aid the design of practical devices. However, at this stage of model development, experimental results are still necessary to validate the fidelity of the simulation models. The structural properties of the flame, like those obtained in this work, are useful for the quantitative validation and comparison with models. In particular, several DNS works have been published in studying different geometries of flames including Bunsen-type flames [10], the same type of burners used in this work.

1.2 Flame Surface Density and Curvature

Flame surface density is defined as the reaction layer surface area per volume. Several approaches for determining the flame surface density have been proposed and explored in the past. One approach to determine flame surface density is a simple algebraic solution introduced by the Bray-Moss-Libby model. The Bray-Moss-Libby model is based on the contours of the spatial distribution of the mean progress variable, (c) [8]. Unburned gases and burned gases correspond to c values of 0 and 1 respectively. Another approach proposed by Pope [12] for determining the flame surface density is based on the gradient of the mean progress variable (c) across the flame front.

In this study, due to the planar nature of the CH PLIF measurements, the flame surface density measurement was simplified in two-dimensional (2D) space by modeling the flame surface density as the flame surface length per unit area. In order to determine the flame surface length, it was necessary to determine the location of the reaction layer at the flame front. Imaging the reaction layer has been heavily explored through well-established techniques such as Rayleigh scattering and PLIF [2, 13, 14]. Rayleigh scattering techniques have been used to image the flame front due to its strong signal strength. Although unable to measure quantity of individual species, Rayleigh scattering is capable of measuring total number density of the

molecules in the mixture. Under certain assumptions, the Rayleigh signal captured is proportional to temperature. Therefore, temperature fields of the images can be extracted to show gradients in temperature. The temperature fields can then be used to determine contours of the progress variable (c) which varies from 0, meaning unburned gas, to 1, meaning burned gas.

PLIF techniques have also established themselves as a powerful diagnostic tool in combustion [15-17]. Unlike Rayleigh scattering, laser induced fluorescence (LIF) techniques are capable of exciting one specific species of multiple molecular species depending on the excitation wavelength of the laser beam. Several different molecular species have been used to mark the flame front based on heat release rates and their close proximity to the flame front. One popular choice for flame front detection using PLIF are hydroxyl (OH) radicals. [18, 19]. OH is a popular choice for flame front marking because it is plentiful in combustion and has maximum concentrations near the flame front. However, OH has slight bias towards the products side of the flame front due to its abundance outside the flame front. Another attractive PLIF species is the overlap layer of OH and CH_2O [20] in which the overlap of these combustion products is said to relate well to the peak heat release rate of the reaction layer [21, 22]. CH radicals are also an attractive species for flame front detection since CH radicals only appear in the reaction zone [4, 6, 23].

In this work, the flame front was imaged by excitation of the CH radical. CH typically exists in lower concentrations and it could be more difficult to detect compared to OH. However, there are CH LIF transitions that could offer significant LIF signal, and CH marks a better location of the flame front because CH marks areas of the flame with peak heat release rates. Recent studies have shown that sufficiently strong CH PLIF signal can be attained at an

excitation wavelength of 314.415 nm with laser energies as low as 0.2 mJ/pulse under kHz rates [24]. The studies here implemented this CH PLIF excitation wavelength.

Many studies have covered experimental calculations on flame surface density on Bunsen-type flames [4]. Halter et al. carried out experimental work determining the effects of equivalence ratio and pressure on flame surface density through the method determined by Pope [25]. Gülder et al. [26] also studied flame surface density under several levels of turbulence intensity through OH PLIF where flame surface density was determined by the method proposed by Pope [26]. Studies completed by Huang and Wang have studied flame surface density of premixed flames composed of syngas mixtures [27] as well as premixed CH_4 and H_2 flames [28] through OH PLIF. Under the work completed by Huang and Wang, flame surface density was determined through the ensemble average of the flame front length per unit area. Other computations for flame surface density have been covered by DNS studies on Bunsen-type flames as well [10].

Curvatures of the flame front also play a role in the structure of the flame. In general, the curvature describes the deviation of a curve from being a straight line. In turbulent premixed flames, structure is important since it is related to the burning rate. As an example, the flame curvature helps to give insight on the local flame structure. This flame structure is used to infer how the flame interacts with the turbulent eddies in the turbulent flow field. As a result, the understanding of the burning velocity in relation to the turbulent flow field and flame structure can be investigated. For example, the flame stretch rate plays a significant role in flamelet structure. The flame stretch rate consists of two components: strains due to non-uniformities in the flow field and curvature of the flame front. In addition, according to Bray et al. [7, 8], the stretch factor, I_0, seen in Equation 1 is also dependent on strain and curvature.

Similar to flame surface density, curvature required imaging and visualizing of the flame front. Afterwards, local expressions for curvature are calculated based on the coordinates of the flame fronts and the derivatives of the coordinates with respect to some fixed origin. Typically, the results of curvature are represented as probability density functions (PDFs). Much experimental work has been done on determining curvature in Bunsen flames [5, 13], V-shaped flames [29, 30], swirl type burners [31], and spherical flames [32]. This work focused on the measurements of highly turbulent Bunsen flames that have not been studied before.

1.3 Summary of Objectives and Contributions

The main objective of this work investigates 2D flame surface density and curvature statistics of a recently developed Bunsen-type burner, called the HiPilot burner, through PLIF by excitation of the CH radicals. Previous studies have not studied flame surface density and curvature for the HiPilot burner. Therefore, a precursive analysis of a piloted jet flame was necessary for validating the methods for determining flame surface density and curvature. Furthermore, the jet flame was chosen for validation studies since experimental data on this popular flame is readily available. The contribution of this work helps to gain a better understanding of experimental combustion dynamics in terms of how flame structure affects burning rates, especially for the highly turbulent HiPilot flames. Furthermore, these studies present an additional benefit by providing experimental data that can be used for validating the fidelity of computational models such as DNS and LES studies, which have yet to be applied to the HiPilot flames.

Planar diagnostics have provided significant contributions to the understanding of turbulent premixed combustion. However, the limitation of 2D diagnostics (such as PLIF used here) is the spatial restriction of measurement to a single plane. As a result, information about

other sections of the flame in other planes is unknown. This planar limitation is critical due to the complex nature of turbulent combustion where flame front structure and wrinkling are inherently three-dimensional (3D). Motivated by this need, recent ongoing developments of 3D diagnostics through tomographic reconstruction have demonstrated the ability to make 3D measurements in turbulent flames under kHz rates. In this method, 2D projections are captured from multiple views and are fed as inputs through a tomographic reconstruction algorithm to obtain 3D measurements. This technique has been investigated through chemiluminescence [33-39], laser induced fluorescence [40-42], laser induced incandescence [43], and Mie scattering [44].

Although 3D measurements are ultimately necessary to fully resolve the 3D flame structures, 2D measurements still have valuable contribution for the combustion community. For instance, 2D measurements can be utilized for validation of ongoing 3D studies by comparing planar slices of 3D flame measurements to measurements collected through 2D techniques [36, 45]. Furthermore, past work has shown the possibility of estimating 3D flame properties based on 2D planar measurements. For example, Huang and Wang et al. [46] have demonstrated the ability to make estimations of 3D flame surface density, under symmetry of the flow and other additional assumptions, based on 2D flame surface density measurements.

With the foundation of the objectives set, the rest of the paper is divided into the following chapters. Chapter 2 describes the experimental configuration as well as steps taken to process the output LIF images. Section 2.1 describes and illustrates the experimental arrangement including the optics, cameras, lasers, burner, and etc. Afterwards, Section 2.2 describes the piloted jet burner as well as features of the relatively new HiPilot burner design and the relevance of its importance in this work. Following the description of the setup, Section 2.3 describes the steps taken to process the raw PLIF images. Then, Section 2.4 demonstrates the

image processing methods applied to the piloted jet flames followed by an explanation for determining flame surface density and curvature in Section 2.5. Chapter 3 shows the validation of determining flame surface density through the well established piloted jet flame (Section 3.1). After validation, Section 3.2 explores the flame surface density applied to the HiPilot flames. Chapter 4 covers the validation of the curvature statistics for the piloted jet flames (Section 4.1) as well as the analysis of the curvature statistics for the HiPilot flames (Section 4.2). Finally, Chapter 5 concludes the thesis by summarizing the work accomplished.

Chapter 2 EXPERIMENTAL CONFIGURATION AND IMAGE PROCESSING

With the understanding of the motivations and objectives established, Chapter 2 underlines the experimental configuration used to capture the flame images as well as the steps to process the raw data. Two flow rate conditions for the jet flame and two flow rate conditions for the HiPilot flame are introduced. In addition, the images presented in this chapter show the capability of imaging the reaction layer by CH PLIF. Finally, the methodology of determining the flame surface density and curvature are defined.

2.1 Experimental Arrangement

Figure 2.1 illustrates a schematic of the experimental setup which includes the laser system, optics, camera, and burner. The laser system consisted of a pump laser (Spectra-Physics GCR-170 Nd:YAG) which generated laser beams with a duration of 100 ns under a repetition rate of 10 Hz. The laser beams had a pulse energy of about 13 mJ/pulse. Afterwards, the pumped laser was used to excite a dye laser (Lumonics HD300 dye laser). A frequency-converting unit (FCU), Inrad Autotracker III, was used to double the frequency of the laser pulse generated from the dye laser. The final output wavelength from the laser system was 314.415 nm in the ultraviolet spectral range that could excite the methylidyne (CH) radicals in combustion with good image fidelity [24]. Out of the FCU a series of focusing and expansion optics were used to guide the path of the laser into the target flow. A collimated lens was used to develop the laser beam into a thin sheet with a height of about 50 mm and a thickness of about 0.2 mm. As shown in Figure 2.1, the laser sheet was guided such that it was passed through the central plane of the burner. A Princeton Instruments (PI) Max camera was used to capture the PLIF signal generated from the interaction of the laser and target flame.

A translational stage was used to move the burner assembly. A coordinate system was established with the origin set at the center of the burner. The X axis was defined as the direction along the path of the laser sheet, and the Y axis was defined as the direction perpendicular to the laser sheet. The Z axis was defined in the direction of the flow. In order to quantify the spatial resolution, a calibration target with a grid of equally spaced grates was placed in front of the PI-Max. The nominal spatial resolution of output images was 42 μm/pixel with a total number of 1024x1024 pixels.

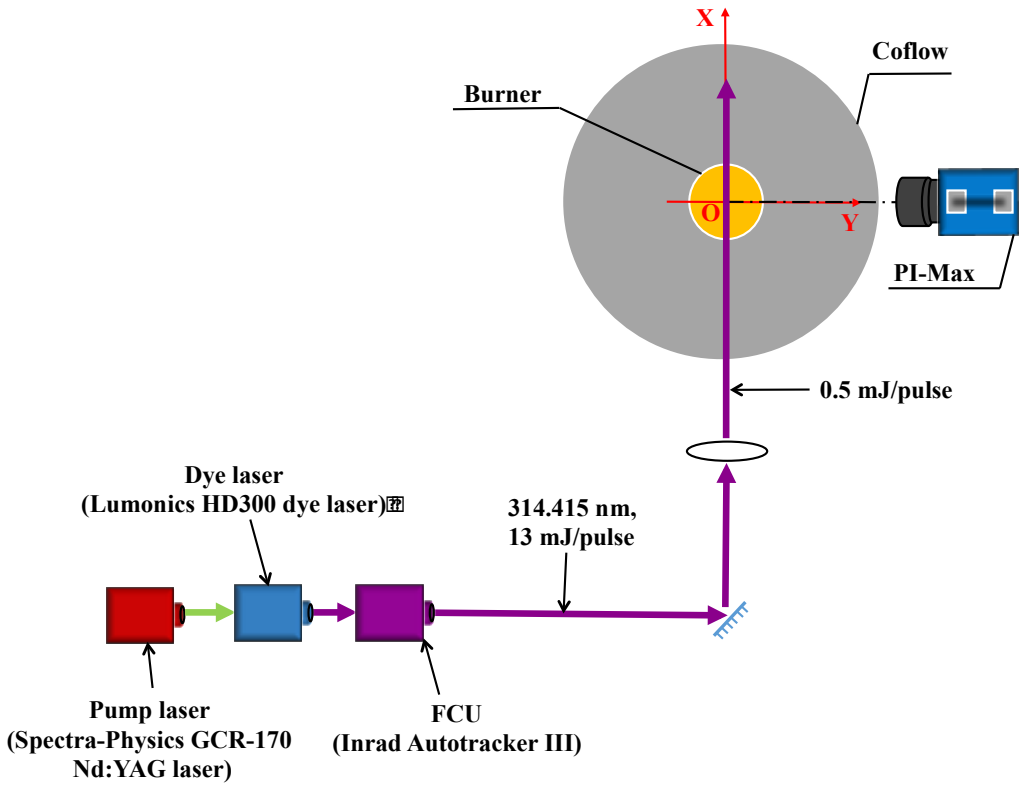

Figure 2.1. Schematic of experimental arrangement.

As previously discussed in Chapter 1, this work tested two different burners that produced two different types of flames. First, a piloted jet burner was used to generate the classical jet flame. Second, the HiPilot burner was used to generate the HiPilot flames. Both the piloted jet burner and HiPilot burner were operated with chemically pure, premixed CH_4 and dry air to produce their respective flames. The ultimate objective in this work was to investigate the

flame surface density and curvature of the HiPilot flames generated by the HiPilot burner. However, it was necessary to validate the methodology of determining these measurements by first studying the classical jet flame because existing data on the jet flame are readily available.

For the piloted jet burner, two different piloted jet flames, labeled B1 and B2, were studied. Flame B1 referred to the flame generated under a lower flow rate, with fuel and air flow rates of 50 standard liters per minute (SLPM) and 5.75 SLPM, respectively. Flame B2 referred to the higher flow rate condition with fuel and air flow rates of 100 SLPM and 11.60 SLPM, respectively. Both the low and high flow rate cases operated under equivalence ratios of 1.05.

For the HiPilot burner, two different HiPilot flames labeled HP1 and HP2 were studied. Both the HiPilot flames studied in this work also operated under an equivalence ratio of 1.05. HP1 referred to the flame generated under a lower flow rate condition with the fuel and air flow rates being 23 SLPM and 212 SLPM, respectively. These conditions had a turbulence intensity, u'/S_L, of 13.4. HP2 referred to the flame generated under a higher flow rate condition with the fuel and air flow rates being 50 SLPM and 454 SLPM, respectively. The turbulence intensity, u'/S_L, for the high flow rate condition was 30.5.

The labeling and summary of the flow conditions studied in this work are shown in Table 2.1. The flow conditions in Table 2.1 include the fuel flow rates, air flow rates, fuel air equivalence ratio, ϕ; mean velocity, U_0; Reynolds number, Re; and the ratio between the velocity fluctuation to laminar burning velocity, u'/S_L, also called the turbulence intensity. The Reynolds number, Re, in this case is defined as

$$Re = \frac{U_0 D}{\nu} \tag{3}$$

where U_0 is the mean velocity at the burner exit, D is defined as the diameter of the burner exit, and ν is the kinematic viscosity.

Table 2.1. Summary of flow conditions

Name	Fuel flow rate (SLPM)	Air flow rate (SLPM)	ϕ	U_0 (m/s)	Re
B1	50	5.75	1.05	11.8	7,385
B2	100	11.60	1.05	23.7	14,785
HP1	23	212	1.05	9.2	12,420
HP2	50	454	1.05	21	28,360

2.2 Piloted Jet Flame and HiPilot Burner

This section provides additional background and discussions of the burners used in this work. Piloted jet flames are a classical example for turbulent premixed flames and have been explored through numerous studies [27, 28, 46, 47]. The piloted jet burner used in this work consists of a primary tube with a 10 mm inner diameter where premixed CH_4 and dry air were discharged. The pilot flame was necessary in order to shield the main flame from effects of the surrounding environment, such as quenching. Furthermore, a 150 mm diameter co-flow was placed around the jet burner which stabilized the flow from the environment.

To simulate the combustion under practical turbulence levels, researchers designed a new burner, named the HiPilot burner, to allow the combustion community to extend the repository of data and analysis to extreme levels of turbulence. Worked done by Skiba et al. [48] showed that the HiPilot burner is capable of producing non-dimensional turbulence intensities from 5 to 185. A few previous studies have been conducted on the HiPilot burner [49, 50] as well as early development in the characterization of the burner [48, 51]. Here some aspects of the burner are described and further extensive information on the HiPilot including a schematic can be found in other published literature [48, 51]. The inner diameter at the exit of the burner is 21.6 mm which

is surrounded by a piloted co-flow with an outer diameter of 108 mm. In order to help generate turbulence, a slotted contraction device was used in the HiPilot burner where the reactants impinged on the slotted plate. Impinging jets can also introduce premixed reactants perpendicular to the main flow to add energy and increase turbulence. Figure 2.2 presents a photograph of the HiPilot burner in operation.

Figure 2.2. Photograph of HiPilot flame.

2.3 Image Processing Methods

PLIF imaging of the target flames was captured in several sections with a field of view of about 43x43 mm^2. Each section was captured along the centerline of the burner nozzle. With the 10 mm jet burner, the CH PLIF images were captured at heights of 0 mm, 40 mm, 80 mm, and

120 mm from the exit of the burner nozzle. Figure 2.3(a) – 2.3(c) shows a sample set of raw CH PLIF images captured for Flame B1. Only images are captured at 0 mm, 40 mm, and 80 mm since the flame front from Flame B1 did not surpass the field of view at 80 mm. The color scales shown in the PLIF images are indicative of the light intensity from the fluorescence of the CH radicals which can be used to back track the concentration of CH. However, for the purposes of this study the color scales are not relevant.

For the HiPilot flames, the HP1 flame images were captured at two heights above the burner exit: 10 mm and 30 mm. The HP2 flame images were captured at 20 mm and 50 mm above the burner exit. For all flames at each section, 300 images were captured and recorded. Figure 2.4 illustrates a sample set of raw CH PLIF images for the two flow rate conditions tested on the HiPilot burner. Figure 2.4(a) – 2.4(b) show raw CH PLIF images from Flame HP1, and Figure 2.4(c) – 2.4(d) display raw CH PLIF images from Flame HP2. As shown from the raw images in Figure 2.3 and Figure 2.4, the flame front was captured by excitation of the CH radicals. In addition, the HiPilot flames from Figure 2.4 were considerably more turbulent than those observed in Flame B1 shown in Figure 2.3. However, the images also contained some noise which must be accounted for.

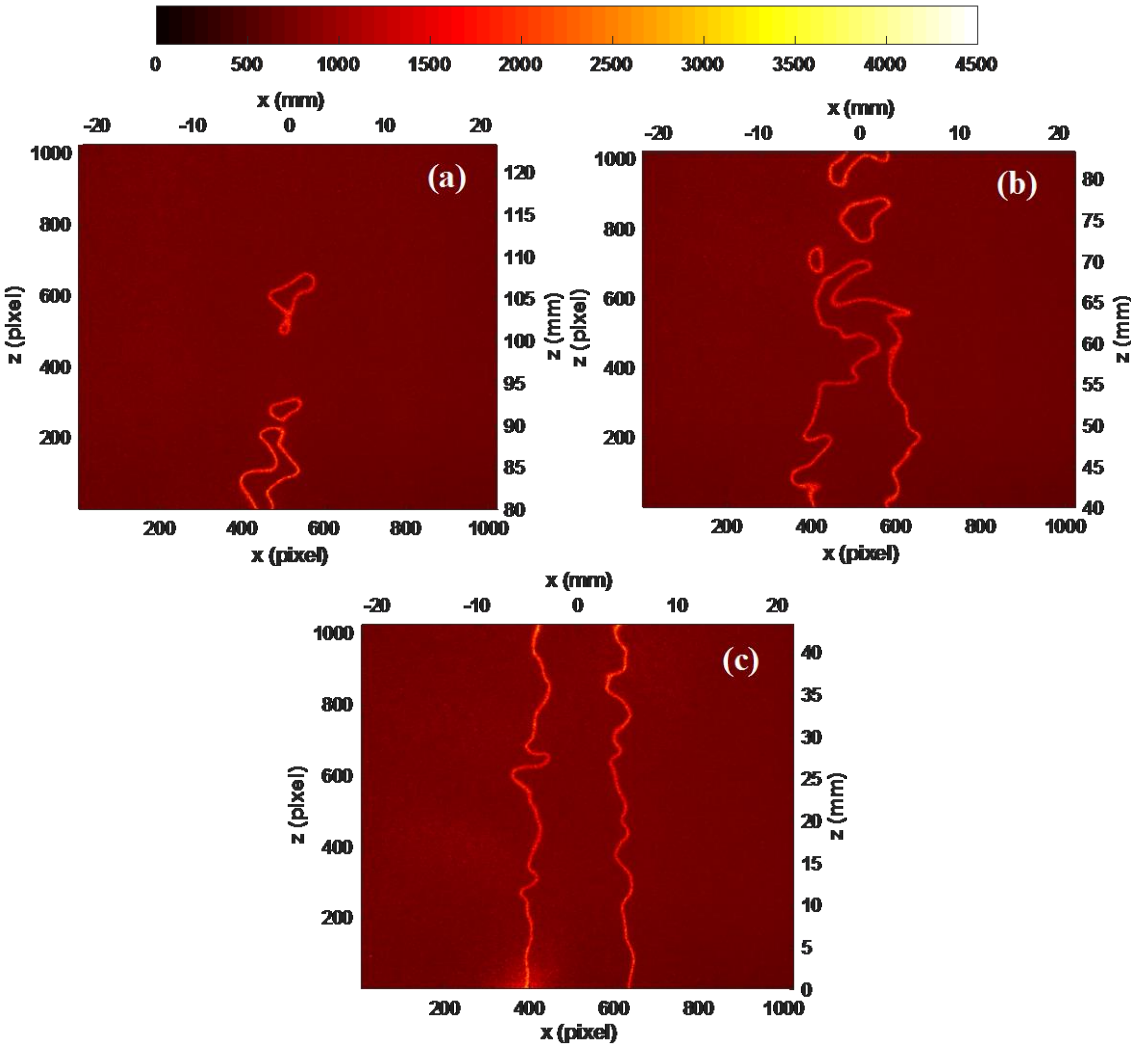

Figure 2.3. Raw CH PLIF images for Flame B1 at heights (a) 0 mm, (b) 40 mm, and (c) 80 mm.

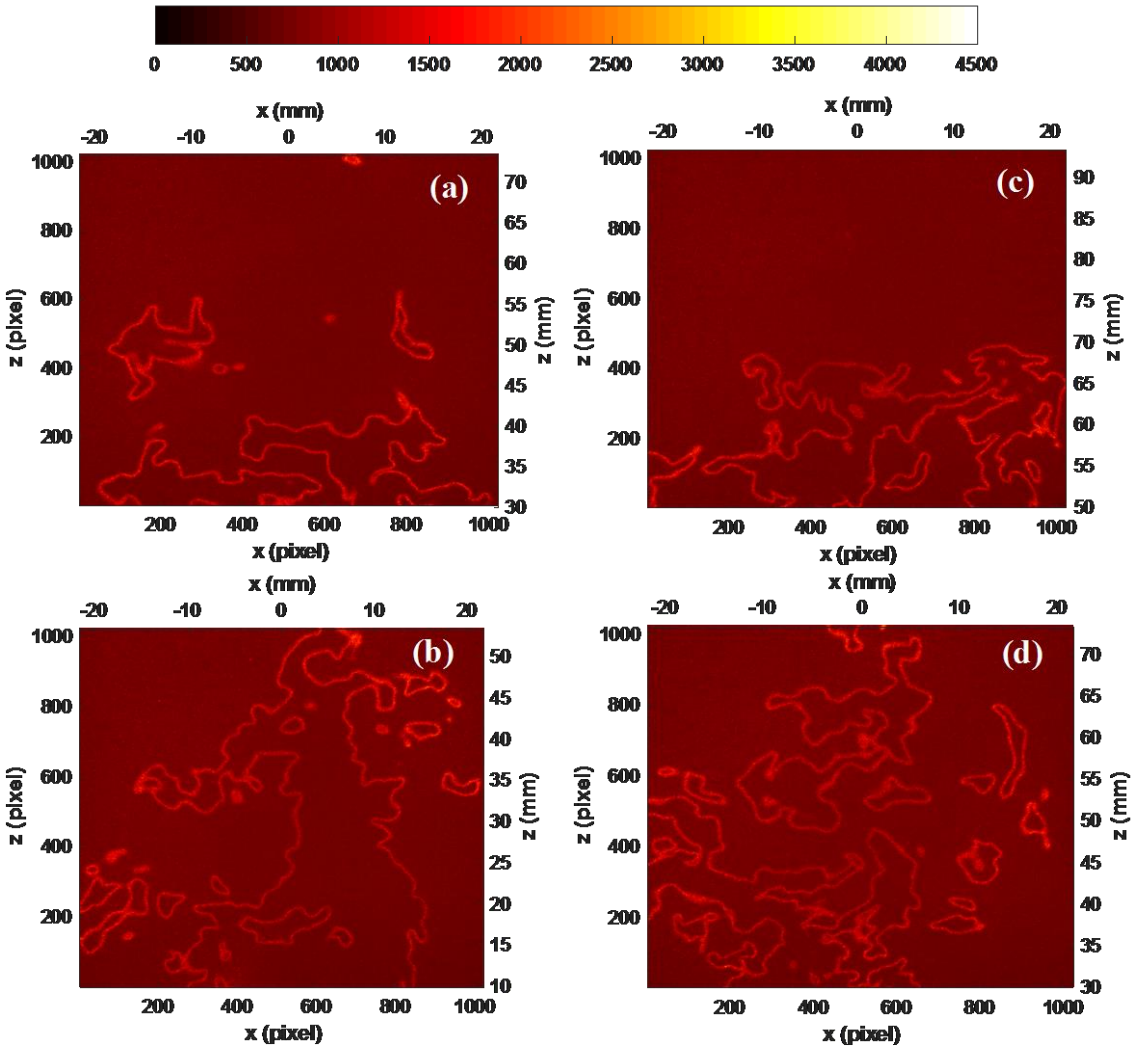

Figure 2.4. Raw CH PLIF images for HiPilot flames, (a) – (b) Flame HP1; (c) – (d) Flame HP2.

The first step taken in processing the images was to subtract the background. Since the raw images consisted of the desired signal and noise in the background, an average background was subtracted to leave the remaining CH PLIF signal. At each height that the CH PLIF images were recorded, 200 frames of the background with the pilot flame on and the main burner off was collected. These 200 frames were condensed into a single image consisting of the average of the intensity values of the 200 background images. The average background was then subtracted from each of the CH PLIF images. Afterwards, the images were binned into 512x512 pixels to further reduce noise (at the cost of reduced spatial resolution of about 0.0846 mm/pixel). Thus,

each pixel in the image covered an area of 85x85 μm^2. Following the binning, a 5x5 median filter was chosen to help remove pixel noise.

The images were then binarized through a local thresholding technique [52]. At each pixel, a neighborhood size of approximately 1/8 of the image size was chosen. The mean intensity in this neighborhood was then calculated. If the intensity of the pixel of interest was lower than this local mean intensity, then the pixel value was set to zero indicating no signal. If the intensity of the pixel of interest was higher than this local mean intensity, then the pixel value was set to one, indicating signal.

Global thresholding techniques, such as Otsu's method [53], were also tried but did not produce binary images as robust as local thresholding. The advantage of locally adaptive thresholding techniques in comparison to global thresholding methods is that local thresholding techniques take into account variations in intensity of an image at different locations. In contrast, global thresholding considers a single global thresholding value based on the entire image.

After binarizing, the thick flame fronts were thinned into lines with widths of one pixel thickness. A parallel thinning algorithm then searched for the flame fronts in the image and deleted pixels layer by layer until a single connected stroke of one pixel wide lines remained [54]. This generated the perimeter of the flame which can be used to determine flame front length and curvature along the flame front.

2.4 Demonstration of Image Processing for Turbulent Jet Flames

To validate the image processing steps described above, I applied them to the well-studied turbulent jet flame. Figure 2.5 shows a sample set of processed images of Flame B1 just before the binarizing step. Figure 2.5 (a) – 2.5(c) correspond to three different heights above the burner. Under the conditions for Flame B1, the fuel and air flow rates were 50 SLPM and 5.75

SLPM, respectively. These flow rates resulted in an equivalence ratio of 1.05 and a Reynolds number of 7,385.

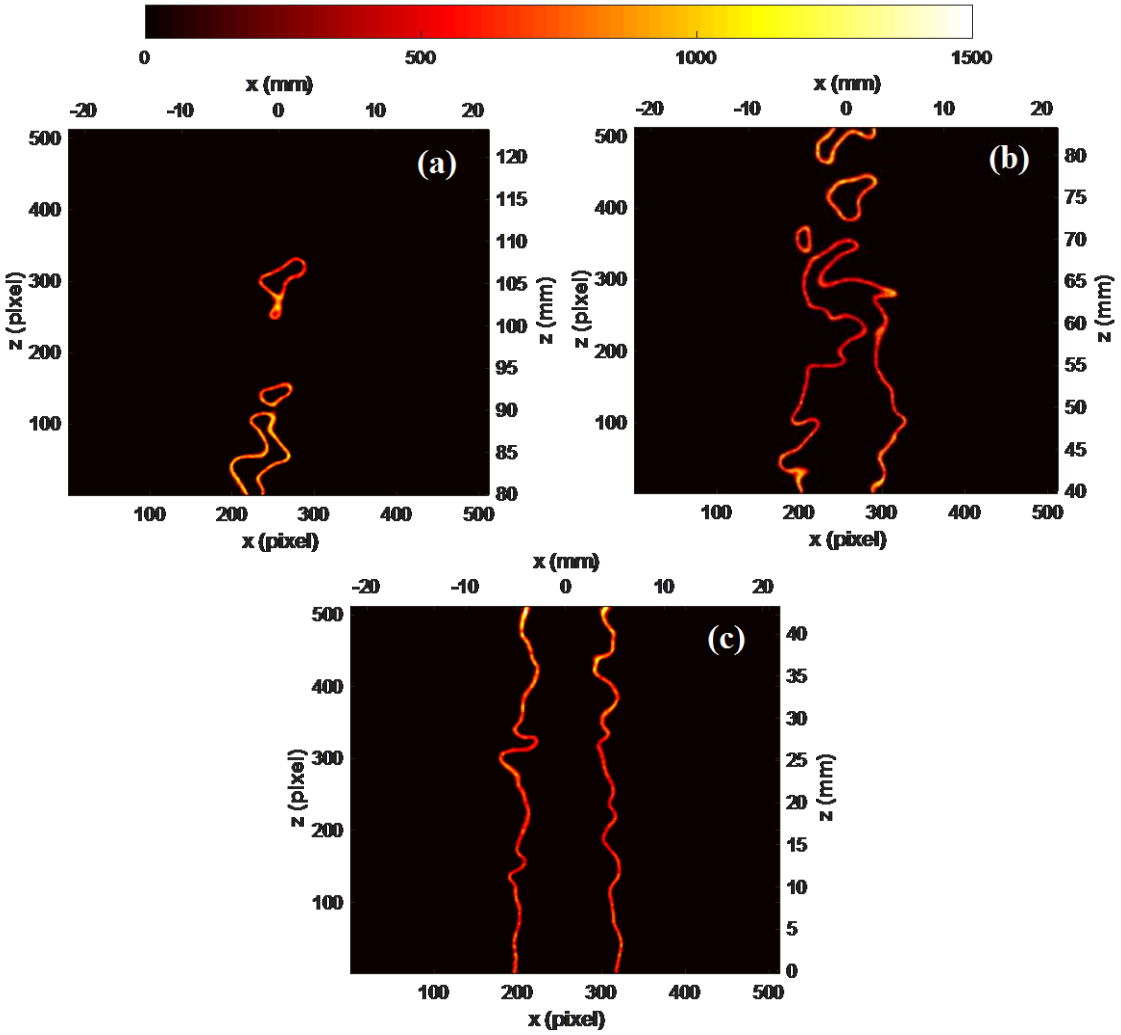

Figure 2.5. Panel (a) – (c) Instantaneous CH PLIF images for Flame B1 at several heights.

A second set of instantaneous CH PLIF images of a turbulent jet flame is shown in Figure 2.6. The images in Figure 2.6 represent the higher turbulent jet flame, Flame B2. Fuel and air flow rates for the higher turbulent jet flame were 100 SLPM and 11.60 SLPM, respectively, resulting in an equivalence ratio of 1.05 and a Reynolds number of 14,785. Figure 2.6(a) – 2.6 (d) shows images taken at four different heights. From Figure 2.6, Flame B2 appeared more turbulent and wrinkled compared to Flame B1 seen in Figure 2.5. Furthermore, Flame B2 was

taller than Flame B1 as broken fragments of the more turbulent flame can be seen at heights as high as 170 mm away from the burner exit.

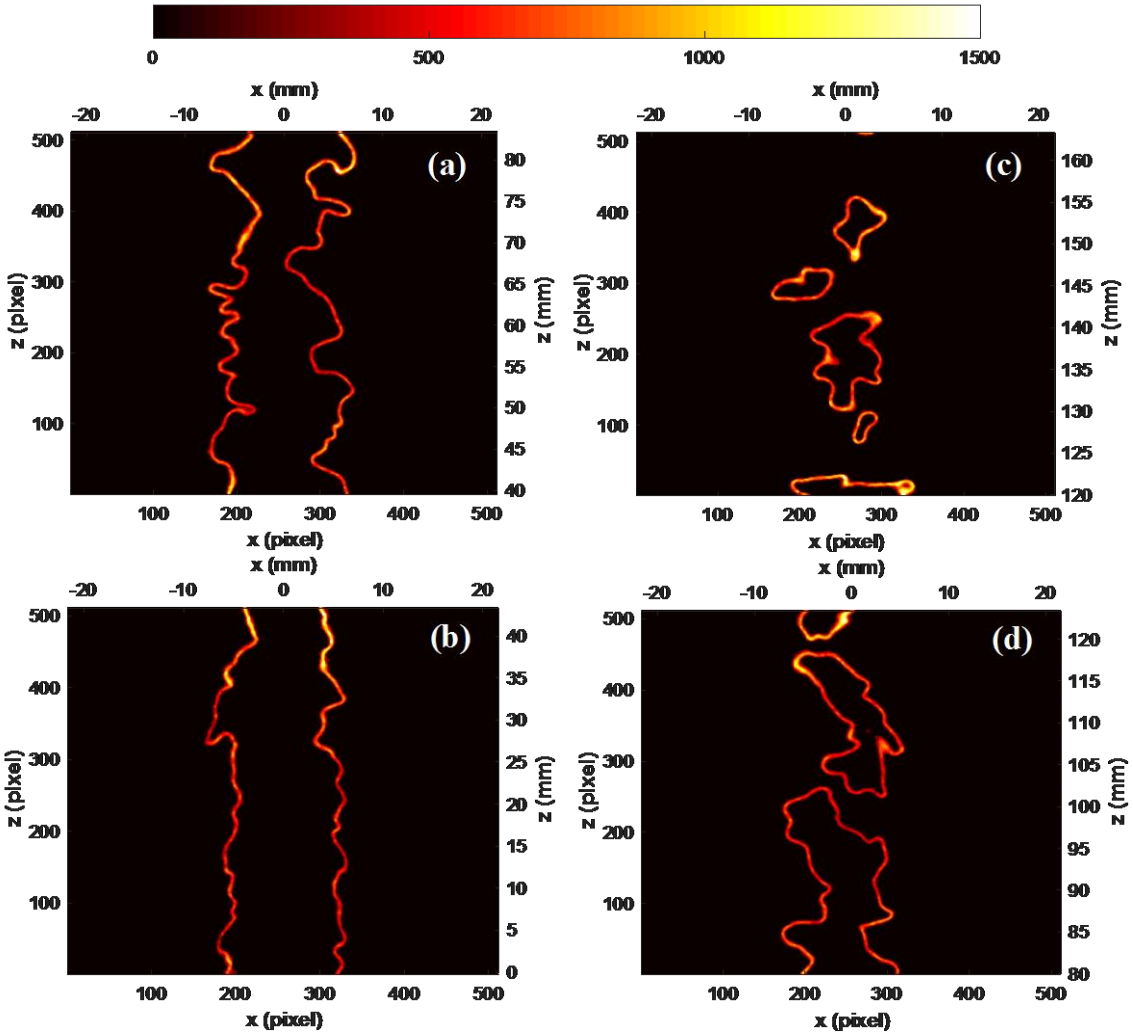

Figure 2.6. Panel (a) – (c) Instantaneous CH PLIF images for Flame B2 at several heights.

In order to determine the flame surface density, the CH PLIF images in Figure 2.5 and Figure 2.6 were converted into binary images and thinned the flame front into a line of pixels with a width of one pixel. The final result of the processed CH PLIF images from the low turbulent jet flame in Figure 2.5 is shown in Figure 2.7. At each pixel, an interrogation box of size Δx^2 (where Δx was defined as the side length of the box) was chosen and the average length of the flame front of 300 frames passing through the interrogation box was determined. The size

of the interrogation box is a parameter that can impact the final statistics; however, the size of the interrogation box insensitively affected the final statistics in this work. I tested interrogation box sizes of 10x10, 20x20, and 30x30 pixels^2 and saw close agreement between the flame surface density fields and profiles. This observation is also in agreement with Filatyev et al. [4] which varied interrogation box sizes between 1.02x1.02 mm^2 to 3.08x3.08 mm^2. In this work, I chose an interrogation box size of 20x20 pixels^2, or 1.70x1.70 mm^2. In order to determine the flame surface density, the average length inside each of these interrogation boxes was divided by the area of the interrogation box.

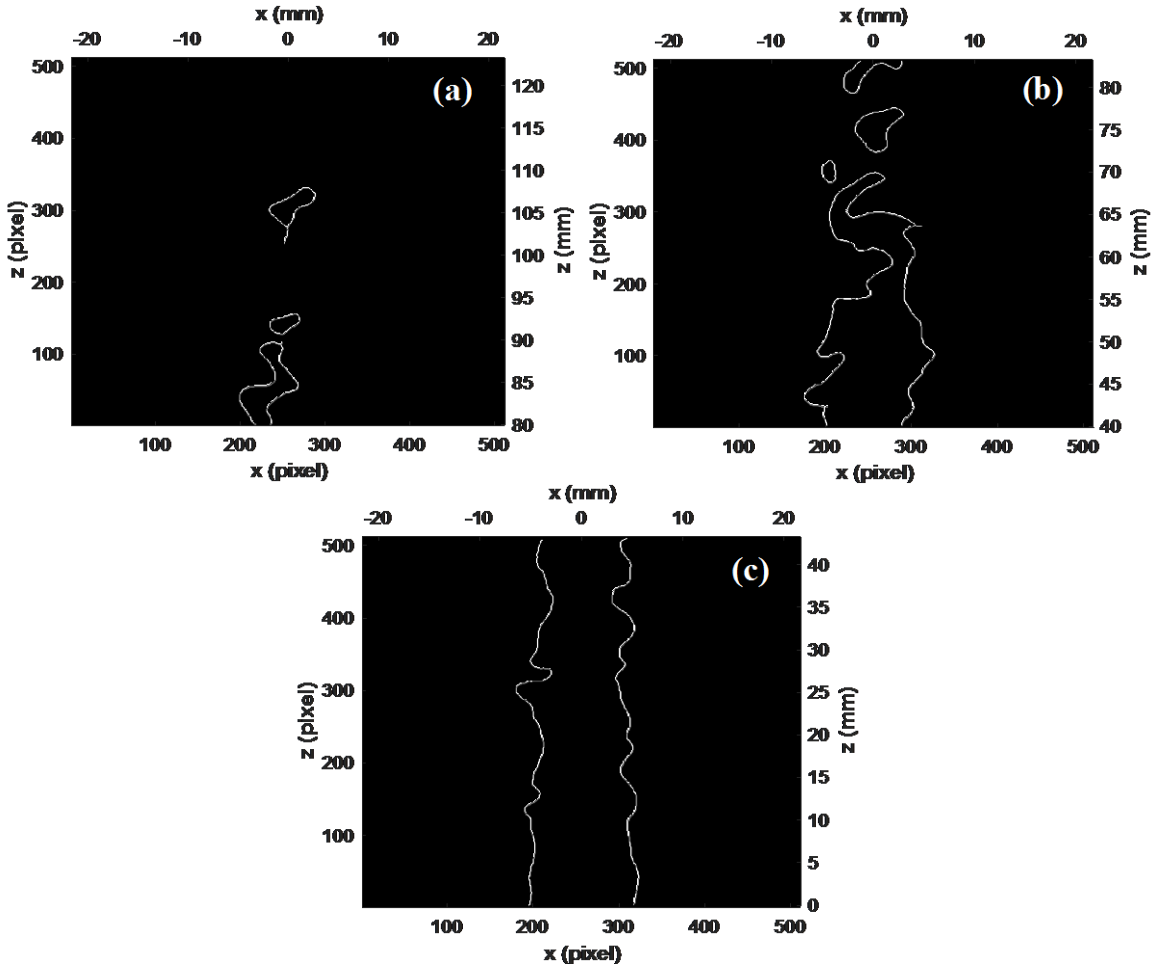

Figure 2.7. Panel (a) – (c) Final result of processed CH PLIF images for Flame B1.

2.5 Methodology for Determining Flame Surface Density and Curvature

The flame surface density is defined as the surface area of the flame front per unit volume. In 2D, the flame surface density can be defined as the surface length of the flame front per unit area (as an approximation of substitution for the 3D flame surface density). Therefore, the flame surface density Σ in the 2D PLIF images can be determined as

$$\Sigma = \frac{\overline{L_f}}{\Delta x^2} \tag{4}$$

where $\overline{L_f}$ is the average length of the flame front within an interrogation box of size Δx. The interrogation box was placed at every pixel and the evaluated flame surface density was placed in the center of the interrogation box.

With the flame front extracted from the CH PLIF images, it was possible to determine the local curvature along the flame front. The local curvature, *k*, is defined as

$$k = \frac{\dot{x}\ddot{z} - \dot{z}\ddot{x}}{(\dot{x}^2 - \dot{z}^2)^2} \tag{5}$$

where *x* and *z* are the coordinates for the position of the flame front. The derivatives of *x* and *z* are taken with respect to the origin in the image. Both a three-point and a five-point finite difference approximation were implemented in order to determine the derivatives. For example the three-point finite difference approximation for $\dot{x}$ and $\ddot{x}$ can be expressed as

$$\dot{x} = \frac{x_{i+1} - x_{i-1}}{2} \tag{6}$$

$$\ddot{x} = \frac{2x_{i+1} - 4x_i + 2x_{i-1}}{2} \tag{7}$$

respectively. Similarly, the five-point finite difference approximation for $\dot{x}$ and $\ddot{x}$ can be expressed as

$$\dot{x} = \frac{-x_{i+2} + 8x_{i+1} - 8x_{i-1} + x_{i-2}}{12} \tag{8}$$

$$\ddot{x} = \frac{-x_{i+2}+16x_{i+1}-30x_i+16x_{i-1}-x_{i-2}}{12} \quad (9)$$

respectively. The index *i* refers to the *i*th point along the flame front. Similar expressions for $\dot{z}$ and $\ddot{z}$ can be made in order to determine the local curvature, *k*. The local curvature was calculated by including only every third pixel from the detected flame front. The four neighbors of every third pixel were then used to calculate the curvature. Positive curvature was defined as being convex to the reactants and negative curvature was defined as being concave to the reactants. This process was completed over 300 different images of the flame.

In order to determine the local curvature, the coordinates of the flame front and their derivatives along the flame front must be known. However, a situation for some images in the set occurred in which sections of the flame front were touching became a problem. For example, Figure 2.8 shows a pocket of reactants just before breaking apart from the main flame. The intersection of points made it difficult to determine the curvature. To simplify this particular problem, the flame front was manually separated into pieces, as shown in Figure 2.8. Afterwards, the local curvature was determined along each piece of the flame front.

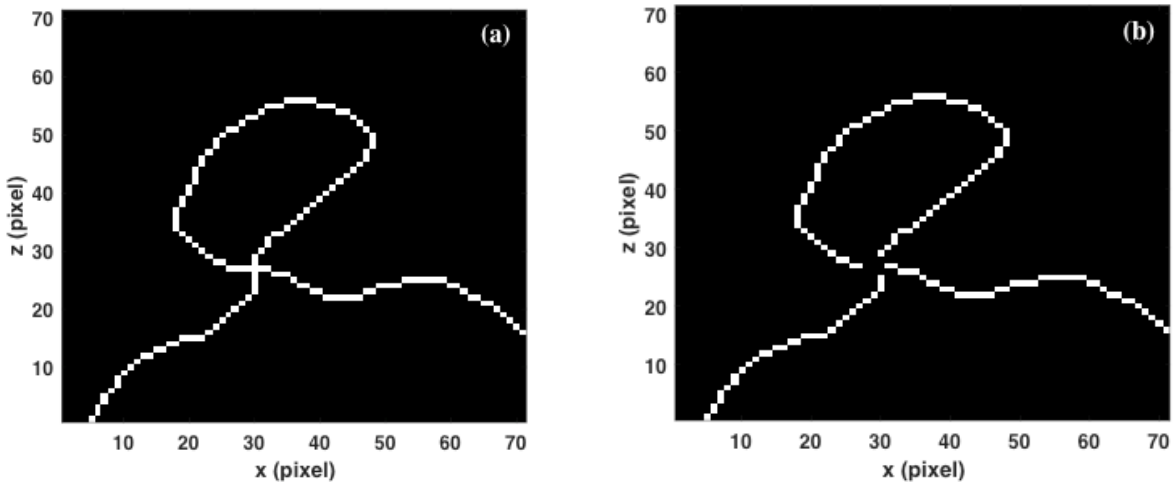

Figure 2.8. (a) Sample image of connected flame fronts. (b) Cut section of flame front.

Chapter 3 FLAME SURFACE DENSITY CALCULATIONS

After the discussion and definition of flame surface density described in Chapter 2, Chapter 3 establishes confidence in the flame surface density calculation by applying the technique to the turbulent jet flame. With plentiful data available on the jet burner, the flame surface density calculations on the jet flame were validated against other published work. By establishing this confidence, the flame surface density was then determined on the HiPilot flames.

3.1 Validation of Flame Surface Density Calculations from Turbulent Jet Flame

For validation purposes, I compared the flame surface density calculations from my CH PLIF measurements with Huang et al. [28] which used the same method from Equation 4 on a 20 mm jet flame and used OH PLIF for imaging. Figure 3.1 shows the flame surface density along a normalized height above the exit burner. The normalized height was defined as the ratio of the height above the burner by the height of the flame brush. In this case, the height of the flame brush was defined at the maximum height where flame surface density was equal to 0.1 mm^{-1}. Thus, the height of Flame B1 was 97 mm and the height of Flame B2 was 166 mm. Figure 3.1 shows the flame surface density profiles at a normalized height of 0.55, or at 53 mm for Flame B1 and 90 mm for Flame B2. The flame surface density was normalized by the maximum value of the flame surface density along the normalized height. Finally, the distance from the burner axis, x, was normalized by the diameter of the burner, D.

The trends in flame surface density from Figure 3.1 between Flame B1 and Flame B2 from the CH PLIF measurements were similar to the measurements studied by Huang et al. [28]. At a normalized height of 0.55, the flame surface density showed two distinct peaks which corresponded to each one of the branches seen in a typical Bunsen jet flame. The differences in

flame surface density are attributed to the differences in techniques and conditions. One of the reasons for the discrepancy was the fact that my PLIF measurements relied on excitation of the CH radical. In contrast, flame front detection by Huang et al. [28] relied on excitation of the OH species. As previously stated, OH PLIF is attractive for flame front imaging due to its abundance in the burned gas and absence in the unburned gas. However, the flame front from OH PLIF may not be reasonable in highly turbulent and chaotic flows. A second reason for the differences in flame surface density measurements was due to the flow conditions. The equivalence ratio of the flames in my work was 1.05 whereas the equivalence ratio for the flame studied in Huang et al. was 0.90.

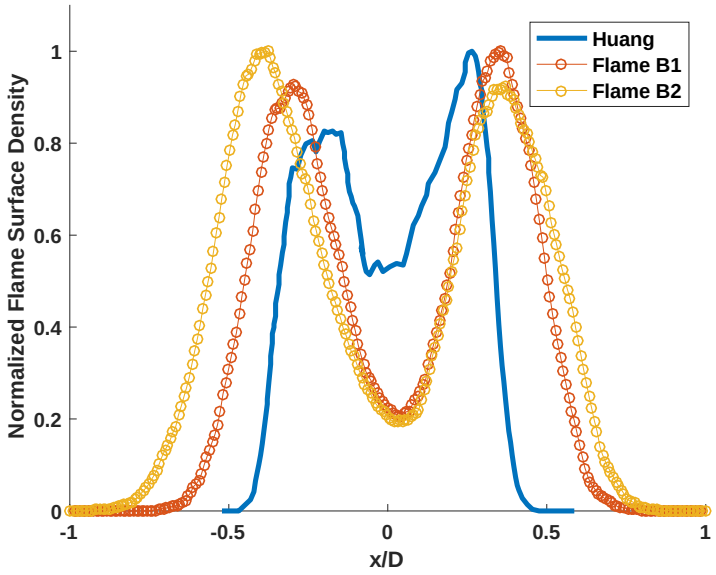

Figure 3.1. Comparison of flame surface density from the turbulent jet flames with measurements from Huang and Wang [28].

The flame surface density fields for Flame B1 and Flame B2 are illustrated Figure 3.2 and Figure 3.3, respectively. The flame surface density fields showed the overall shape of the flame brush averaged over 300 frames. At 40 mm increments along the z-coordinate, the flame showed an abrupt change in flame surface density values. This abruptness was a result of stitching the flame surface density fields on top of each other as the images were captured at

height increments of 40 mm. The two distinct branches of the flame near the burner exit were clearly seen as they merged together to form the tip. Near the burner exit, the flame surface density was at a maximum due to the boundary condition of the flame being attached to the burner. Upwards from the burner, the flame was allowed to move more freely. As a result, the flame surface density profile decreased with height. In addition, Figure 3.2 and Figure 3.3 showed symmetry about the burner axis which was expected for the axisymmetric jet burner.

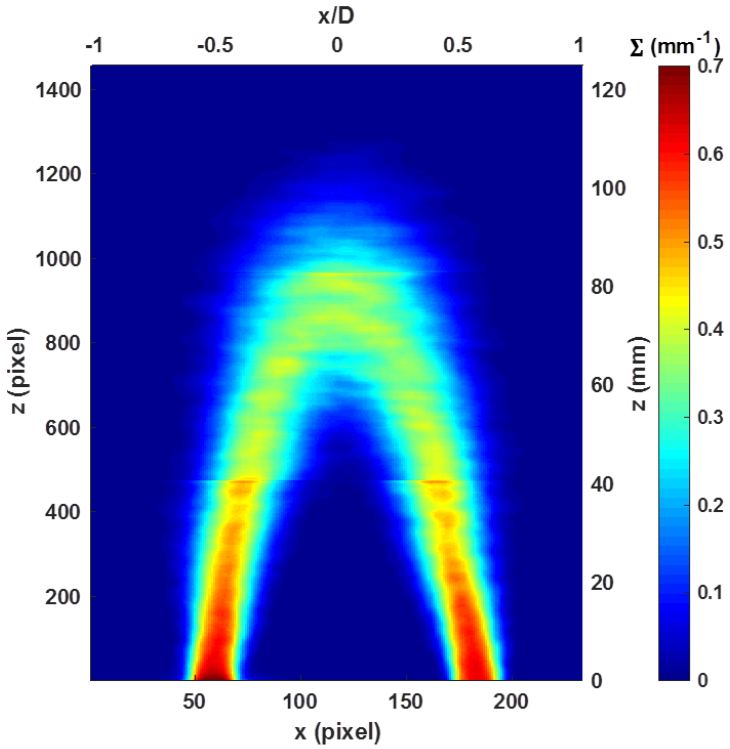

Figure 3.2. Flame surface density field for low turbulent case.

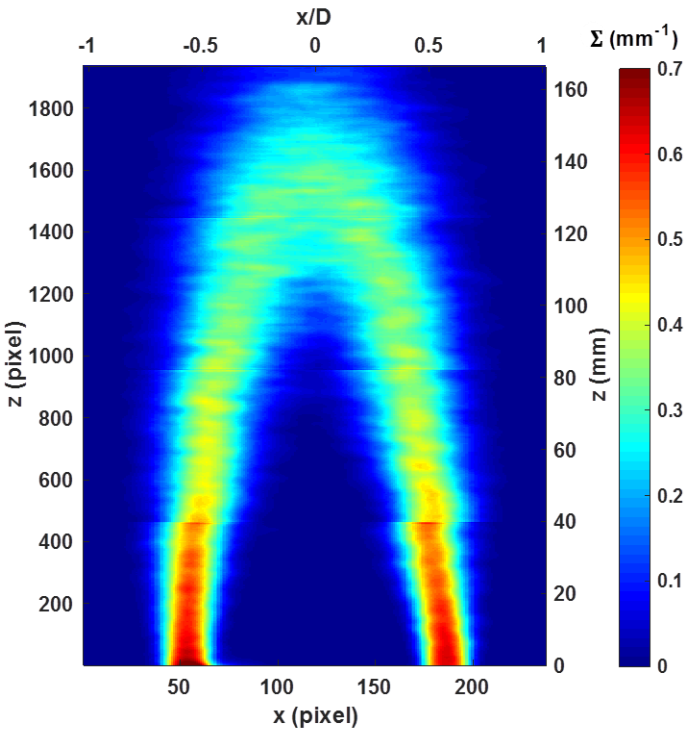

Figure 3.3. Flame surface density field for high turbulent jet.

Figure 3.4 and Figure 3.5 show the profiles of the flame surface density at several heights above the burner exit for Flame B1 and Flame B2 respectively. Near the burner exit, there were two peaks in the flame surface density corresponding to the two branches of the flame. At higher portions of the flame, the two peaks of the flame surface density came closer together and eventually formed a single peak. Similar results of flame surface density fields [27, 28] and flame surface density profiles [4, 10] for these types of flames are covered elsewhere.

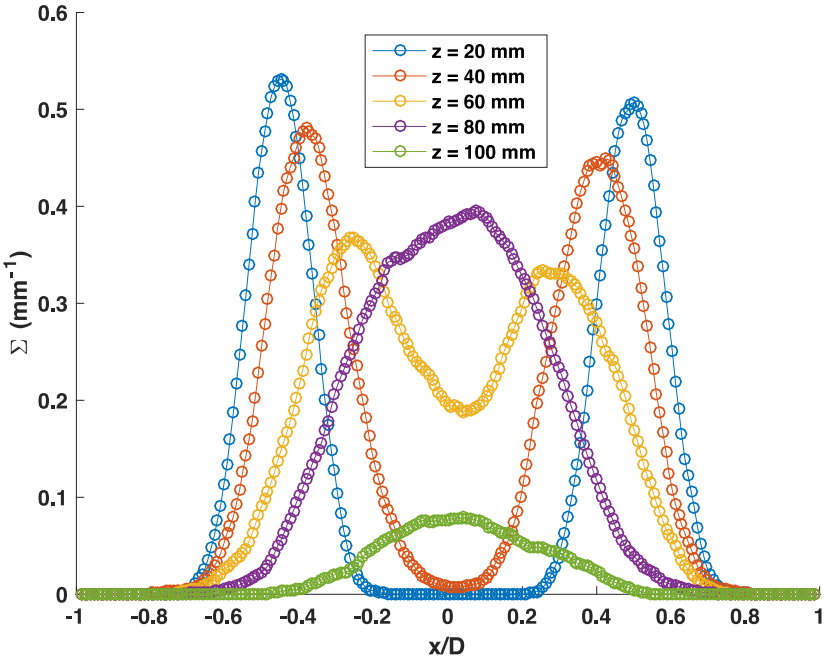

Figure 3.4. Profiles of flame surface density for Flame B1.

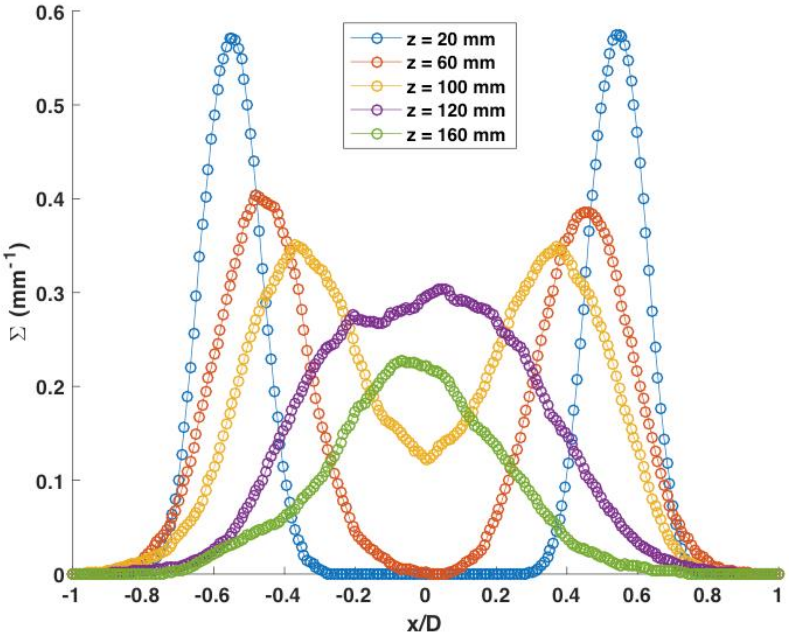

Figure 3.5. Profiles of flame surface density for Flame B2.

3.2 Demonstration of Flame Surface Density Calculations on HiPilot Burner

After validating the method for determining flame surface density, I applied the same image processing techniques on the HiPilot flames. As previously mentioned, the images were binned to 512x512 pixels, and the spatial resolution was 85 μm/pixel. In Figure 3.6(a) – 3.6(b) the raw CH PLIF images for Flame HP1 are shown, and Figure 3.6(c) – 3.6(d) are the corresponding results after imaging processing. Compared to Flames B1 and B2, the HiPilot flame showed longer flame fronts which spanned a wider area due to the larger diameter burner. Similarly, Figure 3.7 shows a sample set of instantaneous CH PLIF images from Flame HP2. Figure 3.7(a) – 3.7(b) illustrate the raw CH PLIF images, and Figure 3.7(c) – 3.7(d) correspond to the same PLIF snapshots after image processing. From the PLIF images of Flame HP2, the qualitative structure of the images was more complicated than Flame HP1 due to the increased level of turbulence. In particular it appeared that the flame front length increased and more pockets of reactants were spread throughout the image when the flow rate was increased.

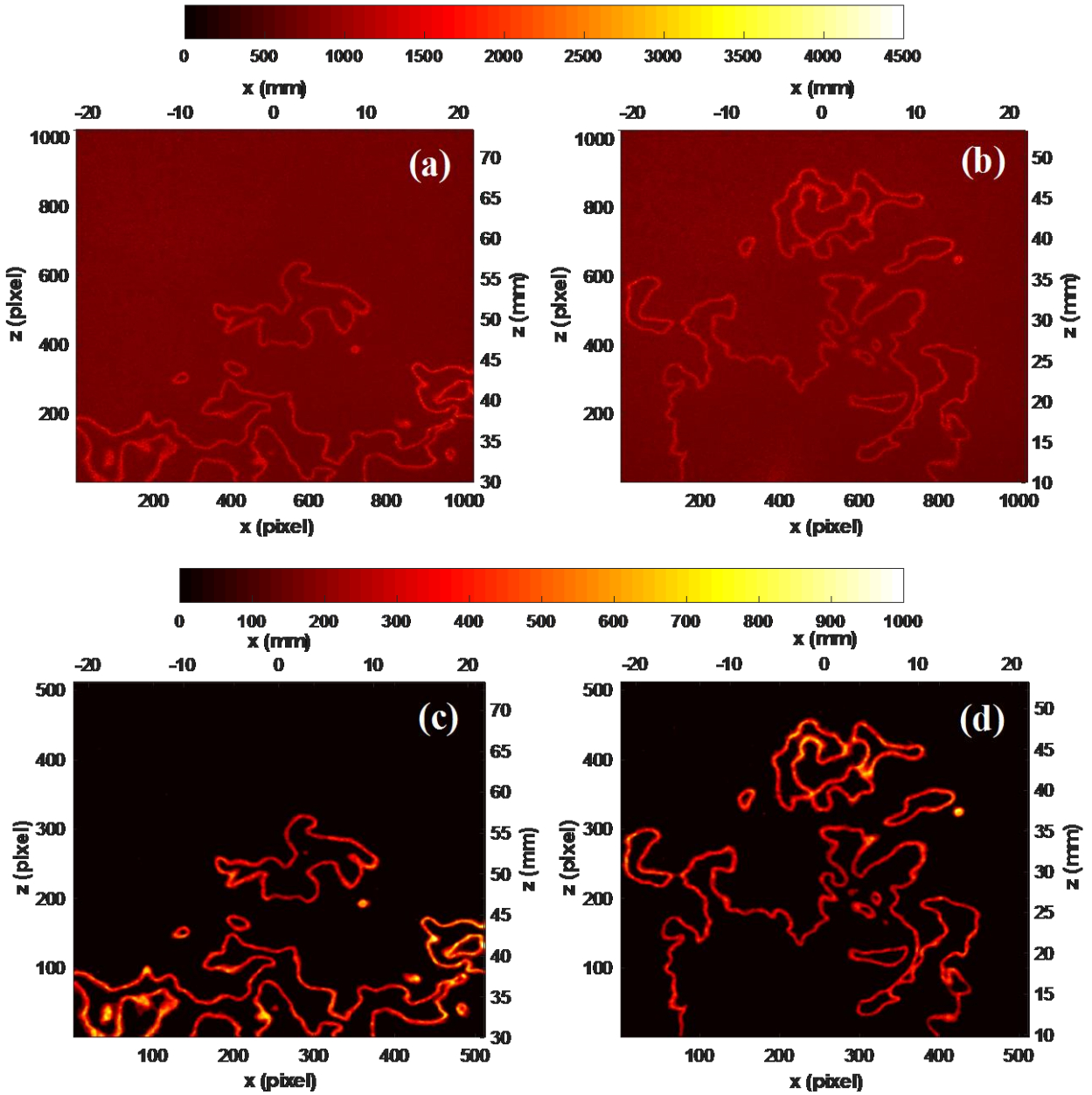

Figure 3.6. CH PLIF images for Flame HP1, (a) and (b) correspond to raw images; (c) and (d) correspond to processed images.

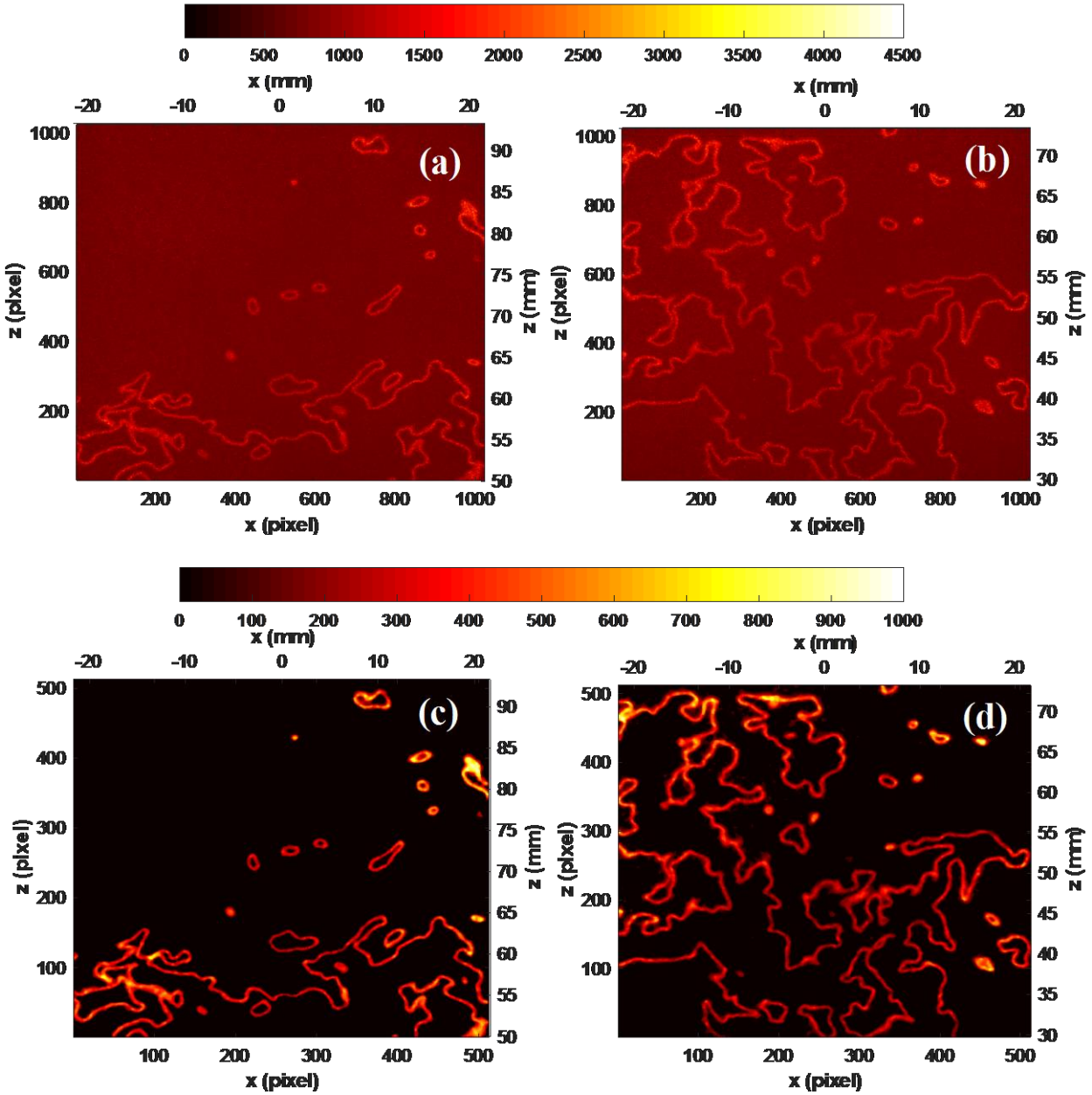

Figure 3.7. CH PLIF images for Flame HP2, (a) and (b) correspond to raw images; (c) and (d) correspond to processed images.

The PLIF images were subjected to the same binarizing and thinning algorithm implemented on the turbulent jet flames. From the thinned flame fronts, the flame surface density fields for the HiPilot flames were calculated. Due to constraints in the experimental set up, imaging for the HiPilot flames was restricted to a minimum height of 10 mm above the burner exit. Figure 3.8(a) – 3.8(b) show the flame surface density field for the lower turbulent Flame

HP1, and Figure 3.9(a) – 3.9(b) display the flame surface density field for the higher turbulent Flame HP2. All flame surface density fields were calculated by using an interrogation box sized 20x20 pixels^2, 1.70x1.70 mm^2 at every pixel for 300 different images.

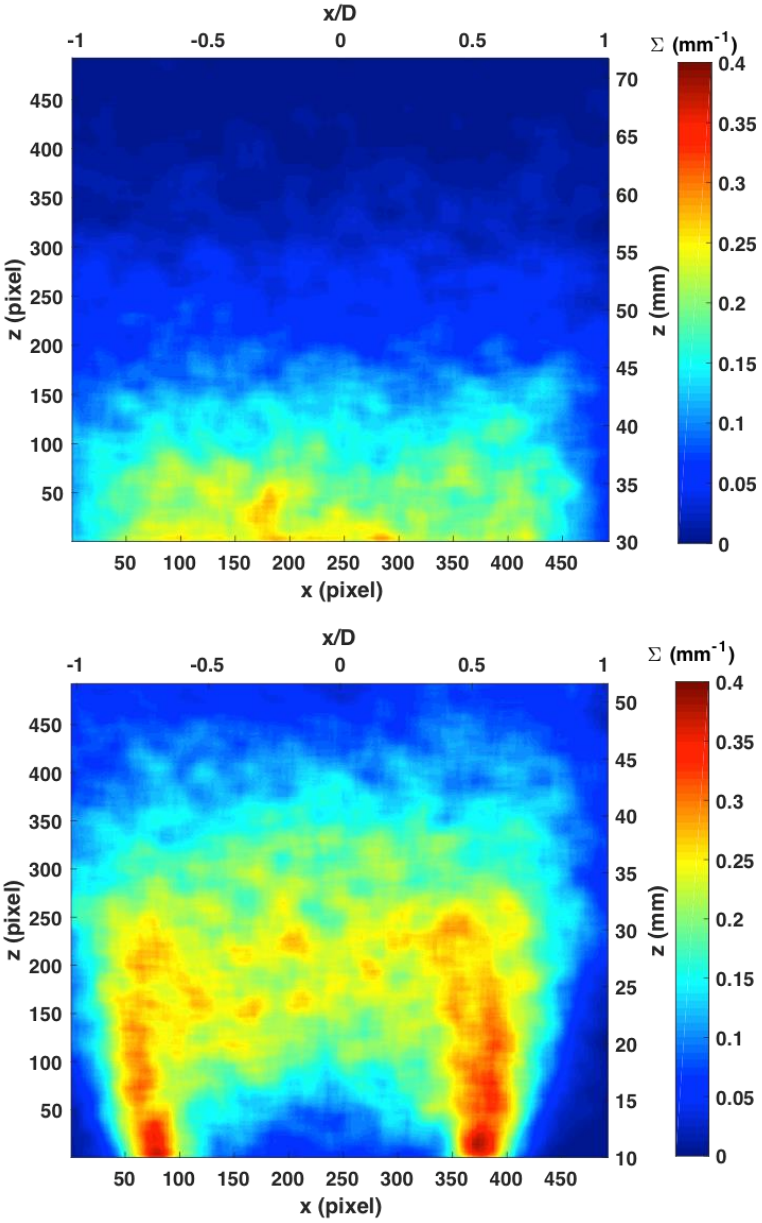

Figure 3.8. Flame surface density field for Flame HP1. Panels (a) and (b) for top and bottom sections respectively.

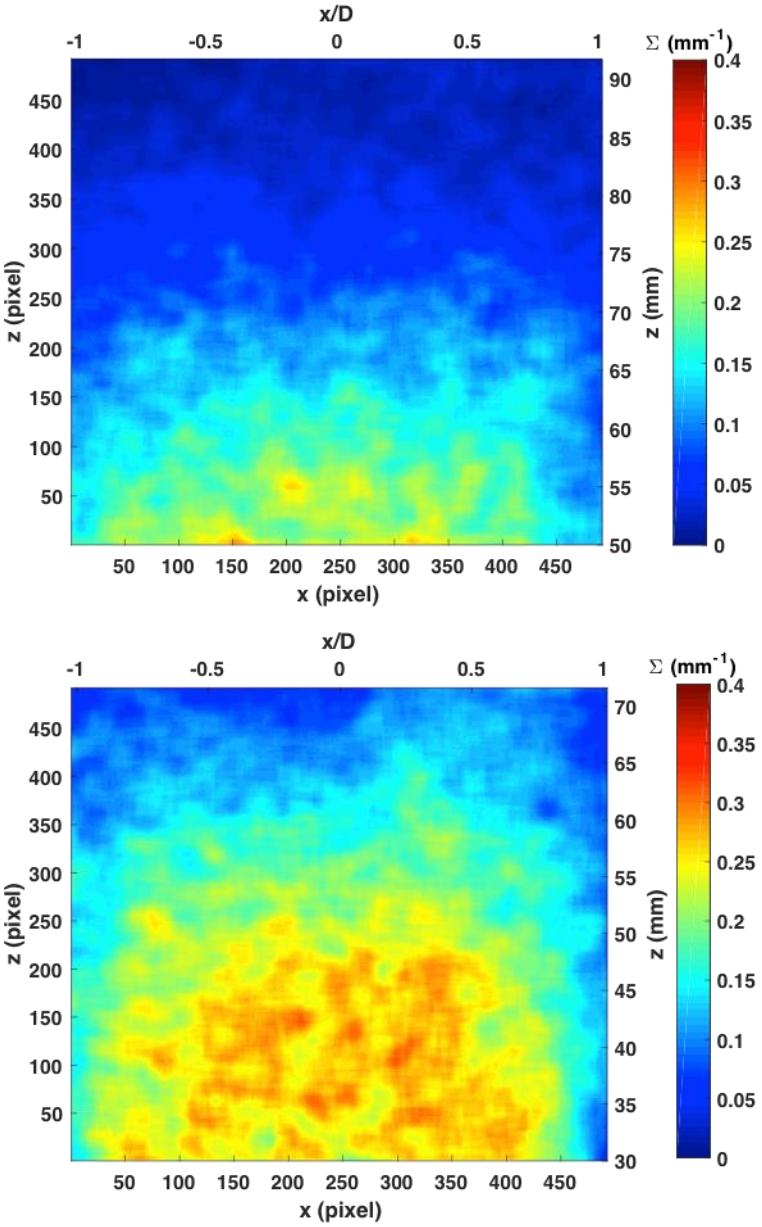

Figure 3.9. Flame surface density field for Flame HP2. Panels (a) and (b) for top and bottom sections respectively.

As expected the HiPilot flame surface density fields spanned a much wider area, and therefore volume, compared to the 10 mm turbulent jet flames. Between Flame HP1 and Flame HP2, the flame appeared to grow in size as it covered a much larger area. In particular, the flame appeared taller for Flame HP2 compared to Flame HP1 as parts of the HP2 flame were seen as high as 90 mm above the burner. Furthermore, Figure 3.8(a) and Figure 3.9(b) show the flame

surface density between Flame HP1 and Flame HP2 at the same height. Although the range of flame surface density values fell between 0 and 0.4 mm^{-1}, Flame HP2 covered a much wider and taller area, and therefore volume, compared to Flame HP1 at the same height.

Figure 3.10 and Figure 3.11 illustrate the flame surface density profiles for Flame HP1 and Flame HP2, respectively, at several heights above the burner. In Figure 3.10, near the burner exit, at 10 mm and 20 mm, the flame surface density profiles exhibited the similar two-peak behavior observed in the 10 mm turbulent jet burner. However, at higher sections of the flame, the flame surface density profiles became lower and wider. The profiles at higher sections of the flame still showed maximum values near the center of the flame brush. However, unlike the 10 mm turbulent jet, the HiPilot flames did not seem to form the Gaussian-like peak observed at downstream locations of the flame.

In Flame HP2, the flame surface density profiles were shown for heights 30 mm above the burner and greater. Therefore, the distinguishable two-peak flame surface density did not appear as in previous conditions. Instead, the flame surface density profiles in Flame HP2 showed a wider profile in which the flame surface density increased towards the burner axis and decreased outward from the burner axis.

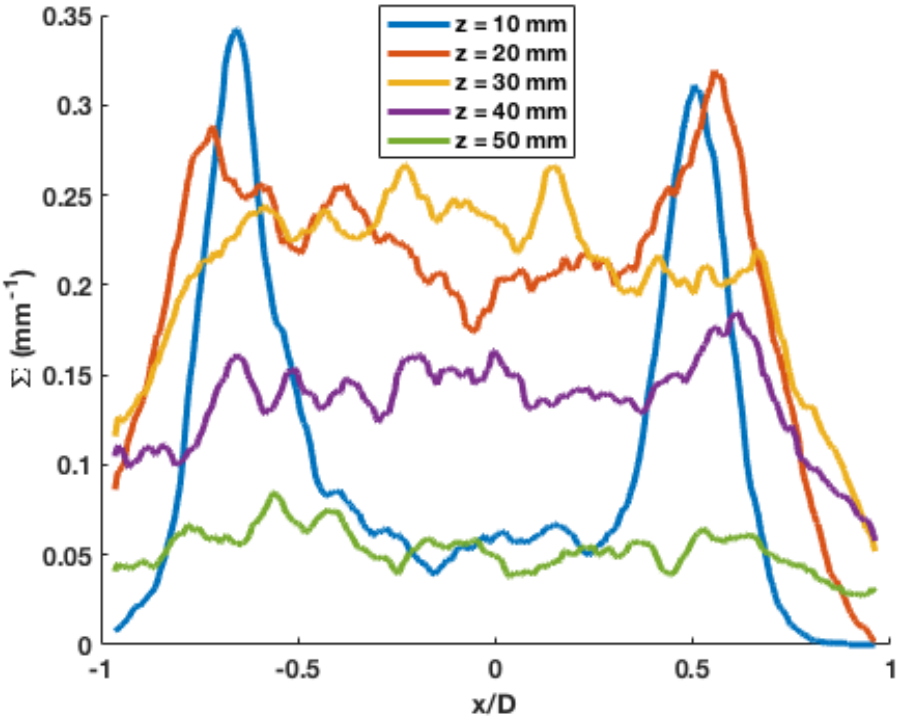

Figure 3.10. Flame surface density profiles for Flame HP1.

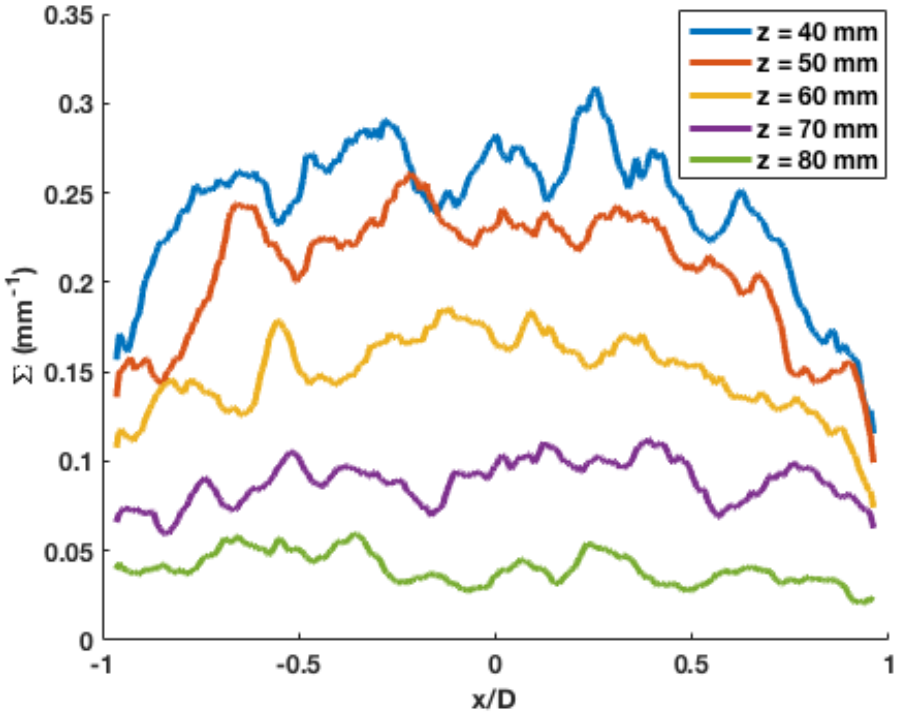

Figure 3.11. Flame surface density profiles for Flame HP2.

Chapter 4 CURVATURE STATISTICS

Before determining curvature statistics on the HiPilot burner, the method of determining curvature was validated through the turbulent jet flame. It has been reported for several flames that the curvature statistics are typically centered around zero and are symmetric about zero curvature. These curvature statistics resemble a bell shape or a Gaussian-like distribution in past studies [5, 32].

4.1 Validation of Curvature Statistics on Turbulent Jet Flame

A brief assessment between the three-point and five-point finite difference methods was completed on the jet flame. Figure 4.1 shows a PDF of the curvature samples and compares the three-point method versus the five-point method. The statistics in Figure 4.1 are from Flame B2 within the field of view from 40 mm to 83 mm. Both methods showed the expected bell shaped distribution. However, the five-point method displayed a smoother distribution that more closely resembled the distributions of other published work on curvature. This is primarily due to the better approximation by including more data from the five-point method to determine the derivatives needed to calculate the curvature. Therefore, the rest of the curvature analysis focused on implementing the five-point finite difference method.

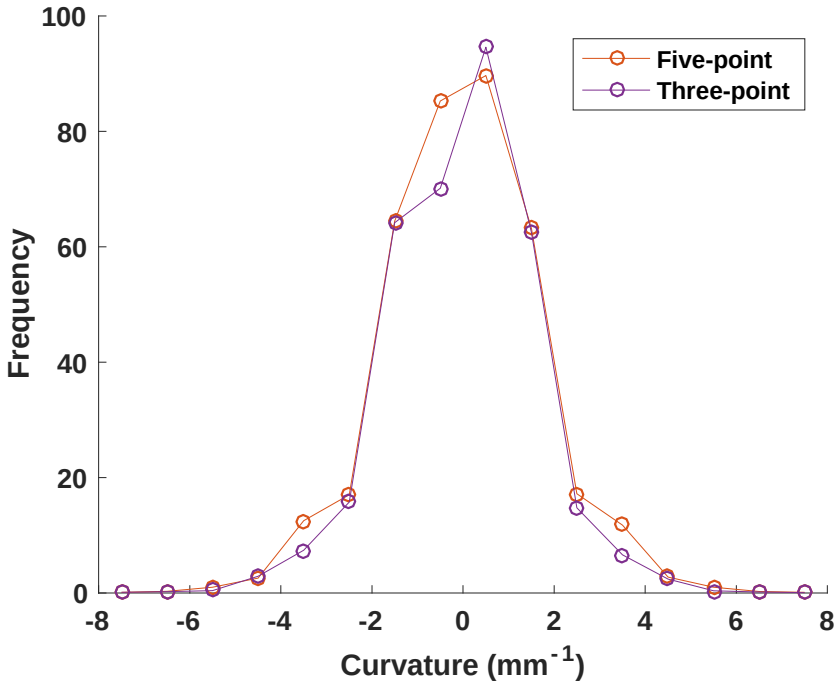

Figure 4.1. Curvature PDF comparison between three-point and five-point finite difference.

Figure 4.2 – Figure Figure 4.5 show the PDFs of the curvature values for both Flame B1 and Flame B2 at several heights above the burner. In particular, Figure 4.3 and Figure 4.4 compares the two 10 mm jet flame conditions to similar work covered by Yuen [47] who used Rayleigh scattering to detect temperature in order to determine the location of the flame front. An 11.2 mm diameter Bunsen burner was used to generate multiple turbulent flames. A turbulent methane and air flame from Yuen, which had an equivalence ratio of 1.0 and a Reynolds number of about 12,250, was chosen for comparison. Flame B1 and Flame B2 had a Reynolds number of 7,385 and 14,785, respectively. Both Flame B1 and Flame B2 had an equivalence ratio of 1.05.

A PDF was created such that the area under the PDF is equal to the number of curvature samples from across 300 frames, divided by 300. Therefore, the area under the PDFs is equal to the average number of curvature samples across 300 images. Figure 4.2 shows the PDF for

curvature at the bottom section of the flame for Flame B1 and Flame B2. The statistics showed that the curvature was centered near zero and had a symmetric distribution of positive and negative curvatures for both flames. This is in accordance with previous experimental work covered in published literature.

Figure 4.3 compares my work with similar work completed by Yuen [47]. The section of the flame covered by Yuen in Figure 4.3 covered from 44.5 mm to 88.5 mm, whereas my PLIF work covered a section of the flame from 40 mm to 83 mm. As shown, the distribution of the curvature results for the turbulent flame displayed a bell shape distribution that was symmetrically centered around zero curvature. The symmetric positive and negative curvature distribution indicates that the flame front curvature has a roughly equal probability of being concave or convex to the reactants. Similarly, Figure 4.4 shows the curvature PDFs for the same set of flames in a field of view from 74.5 mm to 118.5 from work done by Yuen, whereas the work completed here interrogated a of view from 80 mm to 123 mm. The same bell shaped curved distribution centered around 0 mm^{-1} was observed at this height as well. Similar Gaussian-like distributions for curvature were seen at the top section of Flame B2 in Figure 4.5 which covered an area from 120 mm to 163 mm. Only Flame B2 is shown in Figure 4.5 since Flame B1 did not reach this height. Similar bell shaped trends in curvature PDFs were seen under multiple turbulent cases for propane and air flames as well as methane and air flames in work covered by Yuen [47].

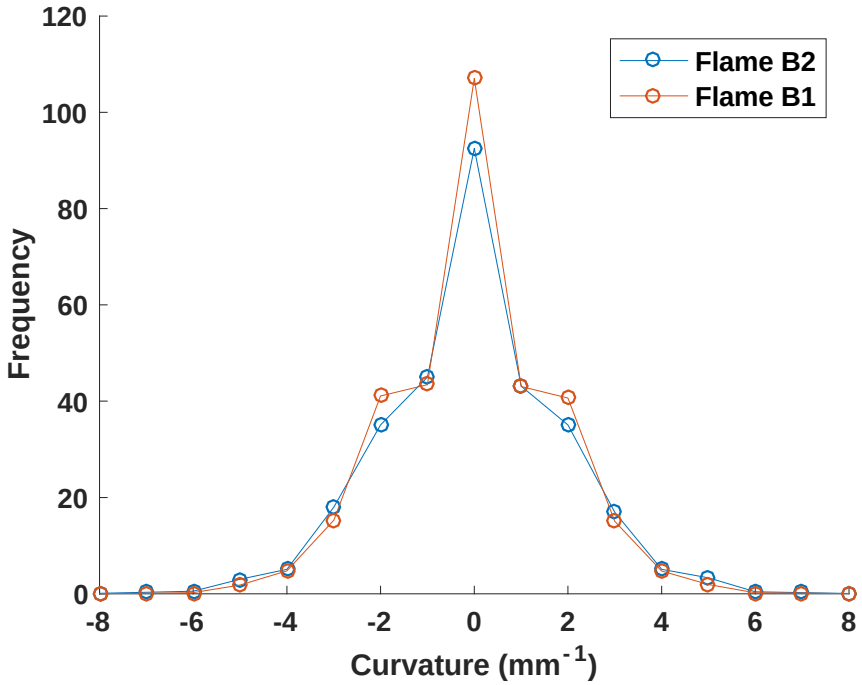

Figure 4.2. Curvature PDF for turbulent jet flames at a height of 0 mm above the burner exit.

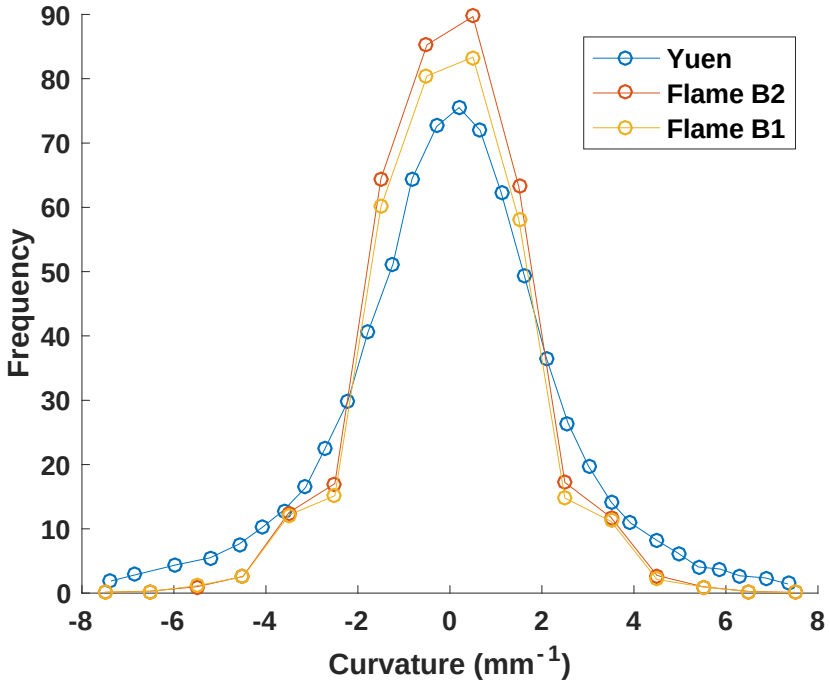

Figure 4.3. Curvature PDF comparison between three turbulent jet flame conditions at a height of above 40 mm above the burner exit.

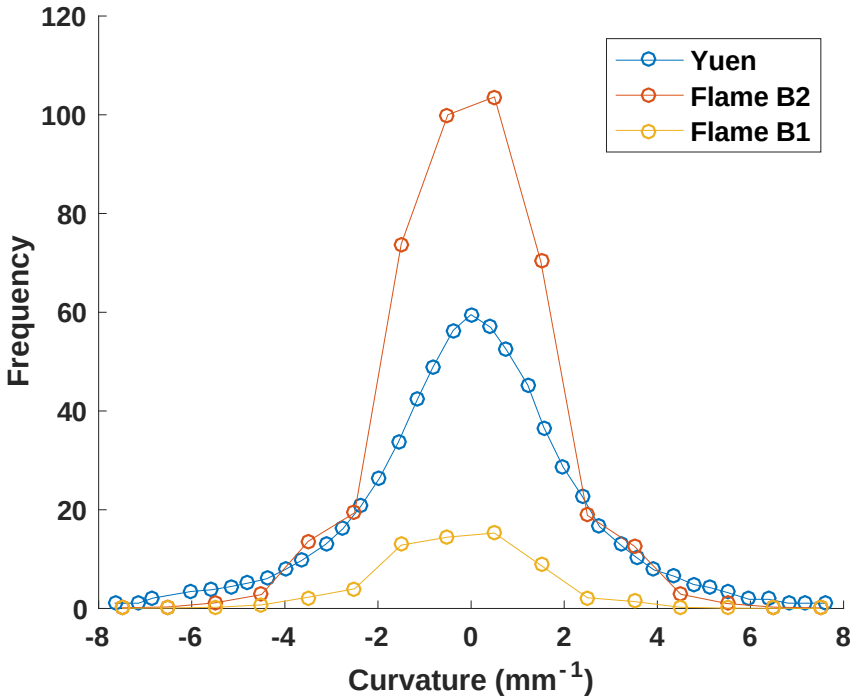

Figure 4.4. Curvature PDF comparison between three turbulent jet flame conditions at a height of above 80 mm above the burner exit.

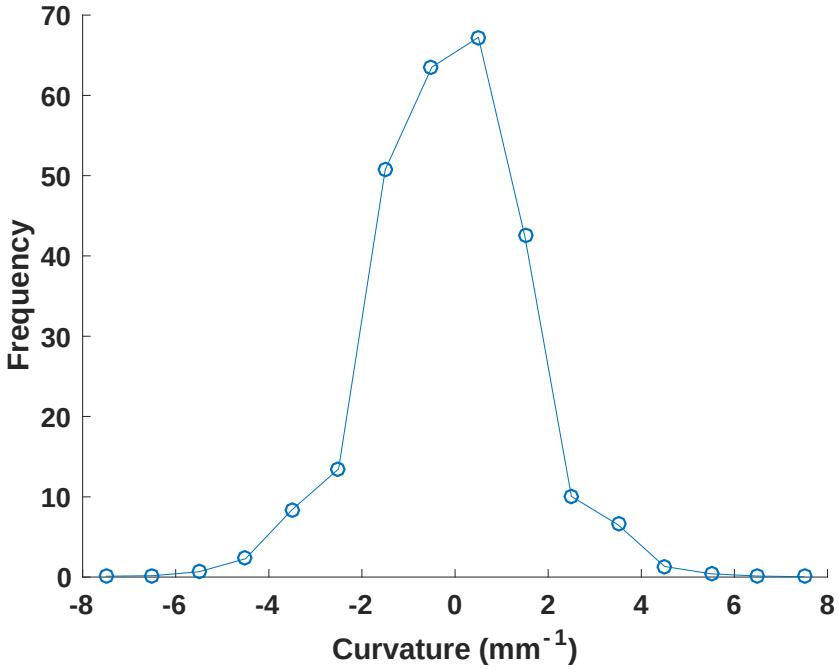

Figure 4.5. Curvature PDF for Flame B2 at a height of 120 mm above the burner exit.

4.2 Exploration of Curvature Statistics on HiPilot Flames

Figure 4.6 – Figure 4.8 show the curvature PDFs for the HiPilot flames. As previously mentioned, the area under the curvature PDF is the average number of sample curvatures per image calculated across 300 images. Figure 4.6 shows the curvature PDF for the bottom section of Flame HP1; Figure 4.7 compares the curvature PDFs for Flame HP1 and HP2 at the same height; and Figure 4.8 shows the curvature PDF for the top section of Flame HP2.

As seen from all curvature PDFs from both HiPilot flame conditions at all heights, the curvature statistics displayed the familiar bell shaped distribution observed in the turbulent jet flames. The distribution for the HiPilot flames was observed to have zero curvature with symmetric distributions for both positive and negative curvature. One particular difference between the curvature PDFs for the HiPilot flames compared to the turbulent jet flames was the frequency counts. More specifically, the bottom sections of Flame HP1, shown in Figure 4.6, and Flame HP2, shown in Figure 4.7, illustrate distributions that are twice as tall as those in seen in the 10 mm turbulent jet flame. This was primarily due to the longer flame fronts, and thus larger sample size observed in the more turbulent HiPilot flames.

Another comparison can be made between Flame HP1 and Flame HP2 at the same height above the burner. Figure 4.7 compares the curvature statistics between the two cases at 30 mm above the burner exit. Although both HiPilot flames displayed Gaussian-like distributions, the Flame HP2 PDF appeared taller due to the longer flame front lengths and wrinkling scales that appeared in the field of view for Flame HP2.

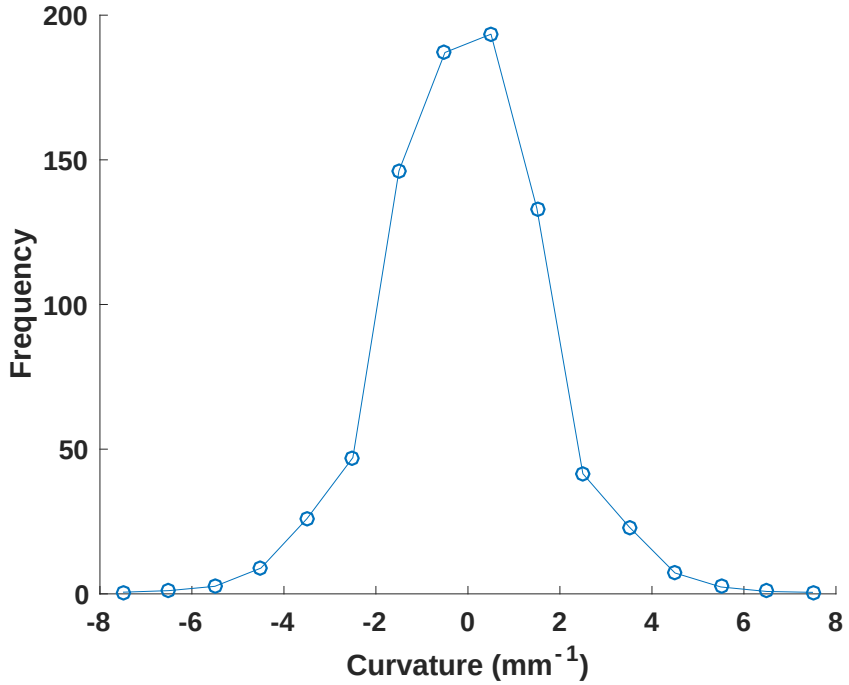

Figure 4.6. Curvature statistics for Flame HP1 at 10 mm from burner exit.

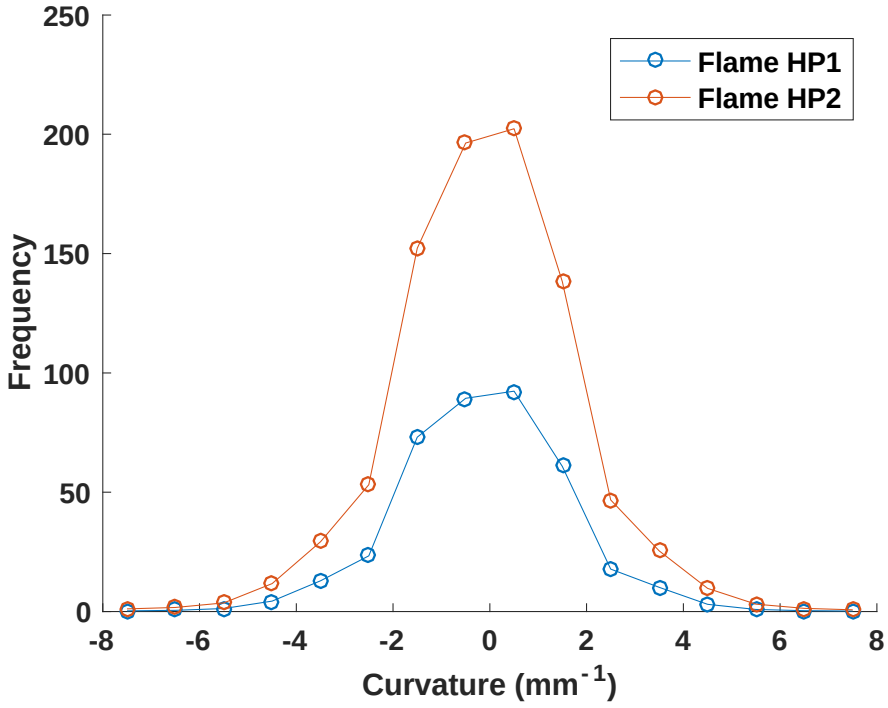

Figure 4.7. Curvature statistics comparing HiPilot flames at 30 mm from burner exit.

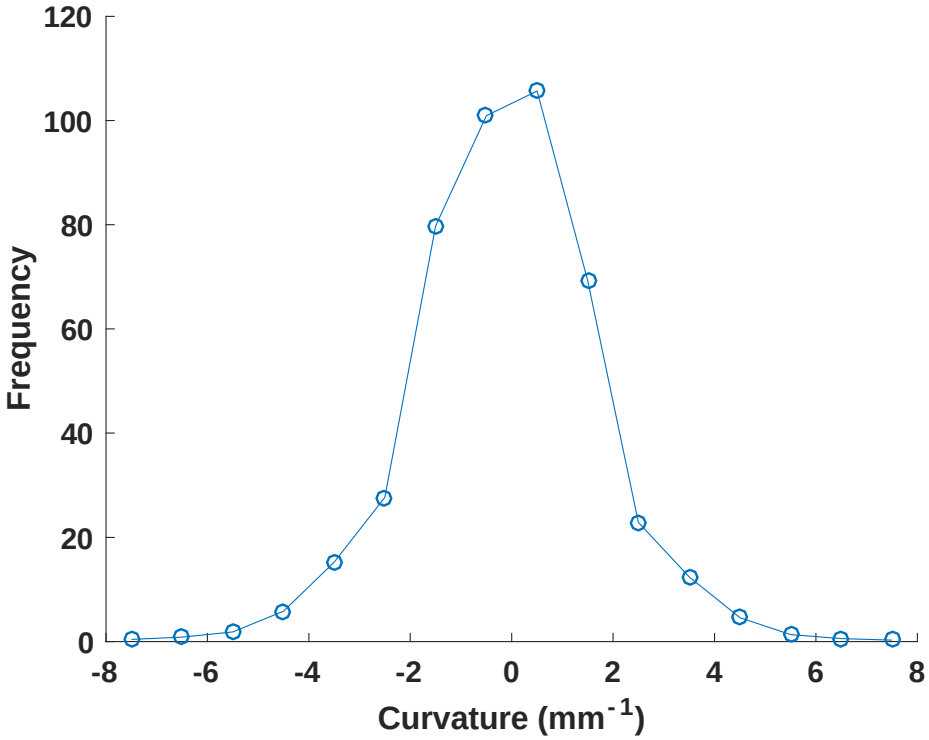

Figure 4.8. Curvature statistics for Flame HP2 at 50 mm from burner exit.

Chapter 5 CONCLUSIONS

This work reports the investigation of 2D flame surface density measurements and curvature statistics for turbulent premixed Bunsen flames. The main contribution of this work is the measurements of these statistics in extremely turbulent flames (generated by the recently developed HiPilot burner) that have not been extensively studied before. The main feature of the HiPilot burner is the ability to create non-dimensional turbulence intensities as high as 185 to simulate turbulence levels expected in some practical applications. For premixed flames, flame structure plays an important role in determining how the flame structure interacts with the turbulent flow fields. Furthermore, the flame structure details how the flame area affects the burning velocity.

Validation of the methods to compute flame surface density and curvature were completed on a turbulent jet flame, which has been studied extensively in literature. The results of the jet flame showed a decrease in flame surface density with height. In addition, flame surface density profiles showed two peaks near the burner nozzle and a single Gaussian-like profile near the tip of the flame. Furthermore, curvature statistics for the jet flame in this work showed symmetric distributions of positive and negative curvatures centered at zero curvature. These flame surface density and curvature observations are in agreement with work completed on other jet flames in literature.

The method of flame surface density and curvature, after the validation discussed above, were applied to the more turbulent HiPilot flames. Flame surface density fields for the HiPilot flames showed that flame surface density decreased with height. Similar to the jet flames, the HiPilot flame surface density profiles showed two peaks near the burner exit. However, the HiPilot profiles showed a wider distribution along the x-coordinate compared to the jet flames.

Curvature PDFs for the HiPilot flames showed a symmetric Gaussian-shaped distribution amongst positive and negative curvatures with a mean curvature near zero indicating roughly equal probability of convex and concave shapes towards the reactants.

Since PLIF techniques were implemented here, only a planar view of the flame front was available. Thus, curvature was restricted to 2D, and the flame surface density definition was reduced from flame surface area per unit volume to the flame surface length per unit area. Future studies could benefit by extending the 2D flame surface density and curvature measurements into 3D and thus provide more information about the flame as a whole. Several recent studies exploring 3D techniques through tomographic reconstruction algorithms have been demonstrated with sub-mm spatial resolution and with temporal resolution under kHz rates. Consequently, ongoing work is being done to analyze the HiPilot burner in 3D to provide information such as 3D flame surface density and curvature measurements.

REFERENCES

1. J. M. Beér, Combustion technology developments in power generation in response to environmental challenges. *Progress in Energy and Combustion Science* **26**, 301-327 (2000).
2. A. C. Eckbreth, *Laser Diagnostics for Combustion Temperature and Species*. (Gordon and Breach Publishers, Kent, U. K., ed. 2nd edition, 1996).
3. J. F. Driscoll, Turbulent premixed combustion: Flamelet structure and its effect on tubulent burning velocities. *Progess in Energy and Combustion Science* **34**, 91-134 (2008).
4. S. A. Filatyev, J. F. Driscoll, C. D. Carter, J. M. Donbar, Measured properties of turbulent premixed flames for model assessment, including burning velocities, stretch rates, and surface densities. *Combustion and Flame* **141**, 1-21 (2005).
5. F. T. C. Yuen, Ö. L. Gülder, Investigation of Dynamics of Lean Turbulent Premixed Flames by Rayleigh Imaging. *AIAA Journal* **47**, 2964-2973 (2009).
6. A. M. Steinberg, J. F. Driscoll, S. L. Ceccio, Measurements of turbulent premixed flame dynamics using cinema stereoscopic PIV. *Experiments in Fluids* **44**, 985-999 (2008).
7. K. N. C Bray, R. S. Cant, Some applications of Kolmogorov's turbulence research in the field of combustion. *Proc R Soc London A* **434**, 217-240 (1991).
8. K. N. C Bray, Studies of the turbulent burning velocity. *Proc R Soc London A* **431**, 315-335 (1990).
9. J. B. Bell, M. S. Day, I. G. Shepherd, M. R. Johnson, R. K. Cheng, J. F. Grcar, V. E. Beckner, M. J. Lijewski, Numerical simulation of a laboratory-scale turbulent V-flame. *Proceedings of the National Academy of Sciences* **102**, 10006-10011 (2005).
10. J. B. Bell, M. S. Day, J. F. Grcar, M. J. Lijewski, J. F. Driscoll, S. A. Filatyev, Numerical simulation of a laboratory-scale turbulent slot flame. *Proceedings of the Combustion Institute* **31**, 1299-1307 (2007).
11. H. Pitsch, D. De Lageneste, Large-eddy simulation of premixed turbulent combustion using a level-set approach. *Proceedings of the Combustion Institute* **29**, 2001-2008 (2002).
12. S. B. Pope, The evolution of surfaces in turbulence. *International Journal of Engineering Science* **26**, 445-469 (1988).
13. F. T. C. Yuen, Ö. L. Gülder, Turbulent premixed flame front dynamics and implications for limits of flamelet hypothesis. *Proceedings of the Combustion Institute* **34**, 1393-1400 (2013).
14. F. Halter, C. Chauveau, I. Gökalp, Characterization of the effects of hydrogen addition in premixed methane/air flames. *International Journal of Hydrogen Energy* **32**, 2585-2592 (2007).
15. R. K. Hanson, J. M. Seitzman, P. H. Paul, Planar Laser-Fluorescence Imaging of Combustion Gases. *Applied Physics B* **50**, 441-454 (1990).
16. I. van Cruyningen, A. Lozano, R. K. Hanson, Quantitative imaging of concentration by planar laser-induced fluorescence. *Experiments in Fluids* **10**, 41-49 (1990).
17. A. Lozano, B. Yip, R. K. Hanson, Acetone: a tracer for concentration measurements in gaseous flows by planar laser-induced fluorescence. *Experiments in Fluids* **13**, 369-376 (1992).

18. M. J. Dyer, D. R. Crosley, Two-dimensional imaging of OH laser-induced fluorescence in a flame. *Optics Letters* **7**, 382-384 (1982).
19. S. D. Hammack, T. Lee, K. -Y. Hsu, C. D. Carter, High-Repetition-Rate OH Planar Laser-Induced Fluorescence of a Cavity Flameholder. *Journal Of Propulsion and Power* **29**, 1248-1251 (2013).
20. P. H. Paul, H. N. Najm, Planar laser-induced fluorescence imaging of flame heat release rate. *Proceedings of the Combustion Institute* **27**, 43-50 (1998).
21. H. N. Najm, O. M. Knio, P. H. Paul, P. S. Wyckoff, A study of flame observable in premixed methane-air flames. *Combustion Science and Technology* **140**, 369-403 (1998).
22. I. A. Mulla, A. Dowlut, T. Hussain, Z. M. Nikolaou, S. R. Chakravarthy, N. Swaminathan, R. Balachandran, Heat release rate estimation in laminar premixed flames using laser-induced fluorescence of CH2O and H-atom. *Combustion and Flame* **165**, 373-383 (2016).
23. J. A. Sutton, J. F. Driscoll, Optimization of CH fluorescence diagnostics in flames; range of applicability and improvements with hydrogen addition. *Applied Optics* **42**, 2819-2828 (2003).
24. C. D. Carter, S. Hammack, T. Lee, High-speed planar laser-induced fluorescence of the CH radical using the $C^2\sum^+$-$X^2\prod$(0,0) band. *Applied Physics B* **116**, 515-519 (2014).
25. F. Halter, C. Chauveau, I. Gökalp, D. Veynante, Analysis of flame surface density measurements in turbulent premixed combustion. *Combustion and Flame* **156**, 657-664 (2009).
26. Ö. L. Gülder, G. J. Smallwood, Flame surface densities in premixed combustion at medium to high turbulence intensities. *Combustion Science and Technology* **179**, 191-206 (2007).
27. M. Zhang, J. Wang, J. Wu, Z. Wei, Z. Huang, H. Kobayashi, Flame front structure of turbulent premixed flames of syngas oxyfuel mixtures. *International Journal of Hydrogen Energy* **39**, 5176-5185 (2014).
28. M. Zhang, J. Wang, Y. Xie, Z. Wei, W. Jin, Z. Huang, H. Kobayashi, Measurement on instantaneous flame front structure of turbulent premixed CH4/H2/air flames. *Experimental Thermal and Fluid Science* **52**, 288-296 (2014).
29. S. Pfadler, F. Beyrau, A. Leipertz, Flame front detection and characterization using conditioned particle image velocimetry (CPIV). *Optics Express* **15**, 15444-15456 (2007).
30. S. Kheirkhah, Ö. L. Gülder, Turbulent premixed combustion in V-shaped flames: Characteristics of flame front. *Physics of Fluids* **25**, (2013).
31. I. G. Shepherd, R. K. Cheng, T. Plessing, C. Kortschik, N. Peters, Premixed Flame Front Structure in Intense Turbulence. *Proceedings of the Combustion Institute* **29**, 1833-1840 (2002).
32. M. Z. Haq, C. G. W. Sheppard, R. Woolley, D. A. Greenhalgh, R. D. Lockett, Wrinkling and Curvature of Laminar and Turbulent Premixed Flames. *Combustion and Flame* **131**, 1-15 (2002).
33. L. Ma, Y. Wu, Q. Lei, W. Xu, C. D. Carter, 3D flame topography and curvature measurements at 5 kHz on a premixed turblent Bunsen flame. *Combustion and Flame* **166**, 66-75 (2016).
34. MW Kang, Y. Wu, L. Ma, Fiber-based endoscopes for 3D combustion measurements: view registration and spatial resolution *Combustion and Flame* **161**, 3063-2072 (2014).

35. MW Kang, X. Li, L. Ma, Three-dimensional flame measurements using fiber-based endoscopes. *Proceedings of the Combustion Institute* **35**, 3821-3828 (2015).
36. L. Ma, Y. Wu, W. Xu, S. D. Hammack, T. Lee, C. D. Carter, Comparison of 2D and 3D flame topography measured by planar laser-induced fluorescence and tomographic chemiluminescence. *Applied Optics* **55**, 5310-5315 (2016).
37. X. Li, L. Ma, Volumetric imaging of turblent reactive flows at kHz based on computed tomography. *Optics Express* **22**, 4768-4778 (2014).
38. X. Li, L. Ma, Capabilities and limitations of 3D flame measurements based on computed tomography of chemiluminescence. *Combustion and Flame* **162**, 642-651 (2015).
39. L. Ma, Q. Lei, Y. Wu, T. M. Ombrello, C. D. Carter, 3D measurements of ignition processes at 20 kHz in a supersonic combustor. *Applied Physics B* **119**, 313-318 (2015).
40. Y. Wu, W. Xu, Q. Lei, L. Ma, Single-shot volumetric laser induced fluorescence (VLIF) measurements in turbulent flows seed with iodine. *Optics Express* **23**, 33408-33418 (2015).
41. B. R. Halls, J. R Gord, T. R. Meyer, D. J. Thul, M. Slipchenko, S. Roy, 20-kHz-rate three-dimensional tomographic imaging of the concentration field in a turbulent jet. *Proceedings of the Combustion Institute*, (2016).
42. L. Ma, Q. Lei, J. Ikeda, W. Xu, Y. Wu, C. D. Carter, Single-shot 3D flame diagnostic based on volumetric laser induced fluorescence (VLIF). *Proceedings of the Combustion Institute*, (2016).
43. T. R. Meyer, B. R. Halls, N. Jiang, M. N. Slipchenko, S. Roy, J. R. Gord, High-speed, three-dimensional tomographic laser-induced incandescence imaging of soot volume fraction in turbulent flames. *Optics Express* **24**, 29547-29555 (2016).
44. D. Ebi, N. T. Clemens, Simultaneous high-speeding 3D flame front detection and tomographic PIV. *Measurement Science and Technology* **27**, 035303 (2016).
45. L. Ma, Q. Lei, T. Capil, S. D. Hammack, C. D. Carter, Direct comparison of two-dimensional and three-dimensional laser-induced flurescence measurements on highly turbulent flames. *Optics Letters* **42**, 267-270 (2017).
46. M. Zhang, J. Wang, W. Jin, Z. Huang, H. Kobayashi, L. Ma, Estimation of 3D flame surface density and global fuel consumption rate from 2D PLIF images of turbulent premixed flame. *Combustion and Flame* **162**, 2087-2097 (2015).
47. F. T. C. Yuen, Doctoral Thesis, University of Toronto, Toronto, Canada (2009).
48. Aaron W. Skiba, Timothy M. Wabel, Jacob Temme, James F. Driscoll, in *54th AIAA Aerospace Sciences Meeting*. (American Institute of Aeronautics and Astronautics, 2016).
49. T. M. Wabel, A. W. Skiba, J. E. Temme, J. F. Driscoll, Measurements to determine the regimes of premixed flames in extreme turbulence. *Proceedings of the Combustion Institute*, (2016).
50. T. M. Wabel, A. W. Skiba, J. F. Driscoll, Turbulent burning velocity measurements: Extended to extreme levels of turbulence. *Proceedings of the Combustion Institute*, (2016).
51. Jacob Temme, Timothy M. Wabel, Aaron W. Skiba, James F. Driscoll, in *53rd AIAA Aerospace Sciences Meeting*. (American Institute of Aeronautics and Astronautics, 2015).
52. D. Bradley, G. Roth, Adaptive Thresholding using the Integral Image. *Journal of Graphics Tools* **12**, 13-21 (2007).
53. N. Otsu, A Threshold Selection Method from Gray-Level Histograms. *IEEE Transactions on Systems, Man, and Cybernetics* **9**, 62-66 (1979).

54. L. Lam, C. Y. Suen, S. -W. Lee, Thinning Methodologies - A Comprehensive Survey. *IEEE Transactions on Pattern Analysis and Machine Intelligence* **14**, 869-885 (1992).